The Astrophysical Journal, 718:739–761, 2010 August 1 doi:10.1088/0004-637X/718/2/739

THE DISTRIBUTION OF STARS AND STELLAR REMNANTS AT THE GALACTIC CENTER

David Merritt
Department of Physics and Center for Computational Relativity and Gravitation, Rochester Institute of Technology, Rochester, NY 14623, USA
Received 2009 September 8; accepted 2010 June 1; published 2010 July 6

ABSTRACT

Motivated by recent observations that suggest a low density of old stars around the Milky Way supermassive black hole (SMBH), models for the nuclear star cluster are considered that have not yet reached a steady state under the influence of gravitational encounters. A core of initial radius 1–1.5 pc evolves to a size of approximately 0.5 pc after 10 Gyr, roughly the size of the observed core. The absence of a Bahcall–Wolf cusp is naturally explained in these models, without the need for fine-tuning or implausible initial conditions. In the absence of a cusp, the time for a $10\,M_\odot$ black hole (BH) to spiral in to the Galactic center from an initial distance of 5 pc can be much greater than 10 Gyr. Assuming that the stellar BHs had the same phase-space distribution initially as the stars, their density after 5–10 Gyr is predicted to rise very steeply going into the stellar core, but could remain substantially below the densities inferred from steady-state models that include a steep density cusp in the stars. Possible mechanisms for the creation of the parsec-scale initial core include destruction of stars on centrophilic orbits in a pre-existing triaxial nucleus, inhibited star formation near the SMBH, or ejection of stars by a massive binary. The implications of these models are discussed for the rates of gravitational-wave inspiral events, as well as other physical processes that depend on a high density of stars or stellar-mass BHs near SgrA*.

Key words: Galaxy: center – Galaxy: evolution – Galaxy: kinematics and dynamics – Galaxy: structure

Online-only material: color figures

1. INTRODUCTION

Near-infrared imaging reveals a cluster of stars around the $\sim 4 \times 10^6\,M_\odot$ supermassive black hole (SMBH) at the center of the Galaxy. Much recent work has focused on the young stars that dominate the total light in the central parsec (Forrest et al. 1987; Allen et al. 1990; Krabbe et al. 1991). These stars have masses of 10–60 $M_\odot$ and appear to have formed in one or more starbursts during the last few million years (Krabbe et al. 1995; Paumard et al. 2006). While their total numbers are small, the density of the young stars increases very steeply toward the SMBH (Genzel et al. 2003; Paumard et al. 2006). How such massive stars can form so deep in the SMBH potential well remains an unsolved problem (Alexander 2005; Paumard 2008).

The dominant population at the Galactic center consists of old stars: mostly metal-rich, M, K, and G type giants with masses of one to a few solar masses (Blum et al. 2003; Davies et al. 2009). The late-type giants dominate the total flux outside the central parsec, and seeing-limited observations as early as the 1960s showed that their surface density follows a power law, $\Sigma \sim R^{-1}$ at $R \lesssim 10$ pc, implying a space density profile $n \sim r^{-2}$ (Becklin & Neugebauer 1968; McGinn et al. 1989; Haller et al. 1996). Inside $\sim$0.5 pc, a drop in the CO absorption strength (Sellgren et al. 1990; Haller et al. 1996) signals a decrease in the projected density of old stars (Genzel et al. 1996; Figer et al. 2000; Scoville et al. 2003; Figer et al. 2003). However, the possibility of contamination by light from early-type stars at these radii made such inferences uncertain.

Three recent studies have clarified the situation. Buchholz et al. (2009) took deep narrowband images of the inner parsec and used a CO absorption feature to distinguish early- from late-type stars. They classified roughly 3000 stars down to a K-band magnitude of $\sim$15.5. Of these roughly 300 were early types, distributed as a steep power law around the SMBH. The late-type stars showed a very different distribution: a core of radius $\sim$0.5 pc, with a constant or even declining surface density inside. Do et al. (2009) obtained higher dispersion spectra of a smaller sample of stars in a set of fields within 0.16 pc from SgrA*, estimated to be 40% complete down to $m_K = 15.5$. They also found a flat or centrally declining projected density of old stars. Bartko et al. (2009b) found a flat distribution of late-type stars with $m_k \leqslant 15.5$ based on spectroscopic identifications in a set of fields in the central 25″.

Inferring the *space* density profile of the old stars from the number counts in the inner parsec is difficult, since the projected density is apparently dominated by stars that are far from the center. But the behavior of the number counts is difficult to reconcile with models in which the space density increases inward. Buchholz et al. (2009) found a best-fit power law of $\Sigma \propto R^{0.17}$ (projected density) for late-type stars inside 6″ and $\Sigma \propto R^{-0.7}$ outside 6″. This corresponds to a space density that drops toward the center, although the counting statistics were also consistent with a flatter profile. Do et al. (2009) inferred a steeper rate of central decline, $\Sigma \propto R^{0.27}$, from their smaller data set, though with larger uncertainties. Do et al. compared the numbers counts with projections of power-law models in $n(r)$ and concluded that the density could not increase faster than $n \sim r^{-1}$ toward the center, although the preferred dependence was shallower.

As the authors of these three studies note, previous descriptions of the stellar density as a broken power law, with $n \sim r^{-1.2} - r^{-1.4}$ inside $\sim$0.4 pc and $n \sim r^{-2}$ outside (Genzel et al. 2003; Schödel et al. 2007), were somewhat misleading, since the counts at small radii were dominated by early-type stars while the counts at large radii were dominated by late-type stars. Presumably, the physical mechanisms responsible for creating these two populations, and placing them on their current orbits, were different and occurred at different times.

Models with a central "hole" naturally resolve one long-standing puzzle: why virial estimates of the SMBH mass based on velocities of late-type stars (Ghez et al. 1998; Genzel et al.

2000; Chakrabarty & Saha 2001; Eckart et al. 2002) gave systematically lower values than the mass inferred from the inner S-star orbits (Gillessen et al. 2009; Ghez et al. 2008). If most of the old stars within the projected central parsec are actually far from the SMBH, their motions will be relatively unaffected by its gravitational force, yielding spuriously low virial masses. Recent studies that explicitly incorporate a low central density for the late-type stars (Zhu et al. 2008; Schödel et al. 2009) yield virial masses for the SMBH that for the first time are consistent with the mass obtained from the orbital fits.

However the low density of old stars at the Galactic center creates new puzzles. A standard assumption has long been that stars near the SMBH should exhibit a cusp in the density, $n \sim r^{-\gamma}$, $\gamma \approx 7/4$. This is the Bahcall & Wolf (1976) solution, which holds for a relaxed (in the sense of gravitational encounters) population of stars moving in a point-mass potential. A number of theoretical studies have argued that the Bahcall–Wolf solution is a robust outcome, depending only weakly on the initial conditions and the range of mass groups present (Murphy et al. 1991; Freitag et al. 2006a; Hopman & Alexander 2006a).

It is possible that a Bahcall–Wolf cusp is present but that the stellar luminosity function changes inside ∼0.5 pc, such that the brightest stars are missing (Buchholz et al. 2009; Do et al. 2009; Bartko et al. 2009b). This could be a result of (physical) collisions before or during the red giant phase, which strip stellar envelopes and keep stars from reaching their peak luminosities (Genzel et al. 1996; Alexander 1999; Bailey & Davies 1999); or tidal interactions between single stars and the SMBH (Davies & King 2005); or it could result from an initial mass function (IMF) that is truncated below $\sim 3\,M_\odot$, since these are the stars that would otherwise dominate the K-band number counts now (e.g., Nayakshin & Sunyaev 2005).

While a "hidden" density cusp is possible, it seems reasonable also to consider models in which the observed stars are representative of the unobserved stars. In these models, both populations would have a relatively low density in the inner parsec. Aside from Occam's principle, a number of other motivations exist for considering such models.

1. *The relaxation time at the Galactic center is long.* The stellar mass density at a distance of 2–3 pc from SgrA*—roughly the SMBH influence radius $r_{\rm infl}$—implies a two-body relaxation time (for solar-mass stars) of 20–30 Gyr. This is the relevant timescale for refilling of an evacuated core if its initial radius is $\sim r_{\rm infl}$.
2. *Stellar kinematics suggest a low mass density in the inner parsec.* Schödel et al. (2009) found that proper-motion data were consistent with a range of models for the distribution of mass in the inner parsec, but the best-fitting models had a flat or declining mass density toward SgrA*, similar to what is seen in the number counts of the old giants.
3. *Physical collisions fail, by a wide margin, to predict the observed depletion of giant stars in the faintest magnitude bins*. Dale et al. (2009) concluded that giants in the $15\,{\rm mag} > m_K > 12\,{\rm mag}$ range would only be significantly depleted within ∼0.01 pc, even assuming a density of unseen colliders (main-sequence stars, stellar-mass BHs) that was four times larger than in the dynamically relaxed models with a Bahcall–Wolf cusp (e.g., Hopman & Alexander 2006a).
4. *Whatever their origin,cores are ubiquitous components of galaxies with SMBHs,* at least in galaxies that are bright enough or near enough for parsec-scale features to be resolved (Ferrarese et al. 2006). Core radii are roughly equal to SMBH influence radii (e.g., Graham 2004), which in the case of the Milky Way would predict a core of radius 2–3 pc.

This paper examines the viability of models for the Galactic center that include a low-density core. Core models are examined first from a structural point of view (Section 2), then from the point of view of self-consistent equilibria (Section 3), and finally from an evolutionary standpoint (Section 4). The basic result is that core models "work": they reproduce the number counts and kinematics of late-type stars, without invoking physical collisions (collisions would be extremely rare in these models) and without the necessity of fine-tuning. We show that a core of the size currently observed is a natural consequence of two-body relaxation acting over 10 Gyr, starting from a core of radius ∼1–1.5 pc; the $n \sim r^{-2}$ density profile outside the core gradually extends inward as the core shrinks and as the stellar density evolves toward, but does not fully reach, the Bahcall–Wolf form after 10 Gyr.

The relaxation time that sets the rate of evolution in these models depends inversely on the mean stellar mass, roughly $1\,M_\odot$ under standard assumptions about the IMF (Alexander 2005). But an old population also contains stellar remnants, including $\sim 10\,M_\odot$ black holes (BHs). In the absence of a core, BHs initially at distances of 4–5 pc from SgrA* would spiral all the way in to the center after 10 Gyr (Morris 1993), potentially dominating the total mass density inside $\sim 10^{-2}$ parsec. In the models considered here, the BH orbits tend to decay no farther than the core radius as determined by the stars (Section 5). The result, after several Gyr, is a rather different distribution of BHs than in the collisionally relaxed models. This difference has potentially important implications for the rates of gravitational-wave-driven inspirals or for other dynamical processes that postulate a dense cluster of BHs around SgrA*, as discussed in Section 6.

The observations motivating this paper are fairly new, and if recent history is any guide, our observational understanding of the Galactic center will continue to change. It is conceivable that the low apparent density of late-type stars is an artifact due to faulty stellar classifications, improper treatment of extinction, confusion, or some other factor. Stars slightly fainter than the current limit for robust detection ($m_K \approx 15.5$) may turn out, once detected, to have a very different spatial distribution, more similar to that predicted by Bahcall & Wolf (1976). Our theoretical understanding of stellar collisions may also change; for instance, new, more effective channels for removal of stellar envelopes could be discovered. Any of these developments would lessen the relevance of the models discussed here to the center of the Milky Way. However, core models are also applicable to other galaxies that contain SMBHs, many of which have cores that cannot plausibly be explained except in terms of a general depletion of stars. And a robust conclusion to be drawn from this work is that the distribution of stars and stellar remnants at the center of the Milky Way should still reflect to some extent the details of the Galaxy's formation—though the imprint of the initial conditions may turn out to be less extreme than in the models considered here.

We assume throughout a distance to SgrA* of 8.0 kpc (Eisenhauer et al. 2005; Gillessen et al. 2009). At this distance, 1 arcsec corresponds to a linear distance of 0.0388 pc and 1 pc corresponds to 25.″78. We also fix the SMBH mass to $4.0 \times 10^6\,M_\odot$ (Ghez et al. 2008; Gillessen et al. 2009).

2. PROPERTIES OF THE STELLAR DISTRIBUTION

2.1. Number Density

As summarized above, a relatively low density of late-type stars near the center of the Milky Way was independently inferred by Buchholz et al. (2009), Do et al. (2009), and Bartko et al. (2009b). The first of these three studies was based on the largest sample of stars, and we adopt the Buchholz et al. number counts as basis for the discussion that follows.

Buchholz et al. (2009, hereafter BSE09) took deep, narrow-band images ($K < 15.5$) in the near-IR K band and distinguished late-type (old) from early-type (young) stars using CO equivalent widths, calibrated from existing samples. Extinction was estimated star by star by comparing observed spectral energy distributions (SEDs) with a blackbody of variable extinction. BSE09 identified a "quality 1" sample consisting of late-type stars in which the CO band depth exceeded the cutoff value for early-type stars by 1σ or more, and which did not fall into any of the other classes defined by them (asymptotic giant branch (AGB) stars, foreground sources, very red objects). The resulting data set contains 2955 stars down to a magnitude limit of $K = 15.5$. Figure 1 shows the BSE09 number counts (their Figure 11) plotted versus projected distance from SgrA*.

The BSE09 data are believed complete to a limiting magnitude $K = 15.5$ within a projected distance of $\sim 20''$ from SgrA*. Beyond this radius, the early-type stars are insignificant in numbers compared with the late-type stars. Schödel et al. (2007) present total number counts in a more extended region, derived from the ISAAC NIR camera on the Very Large Telescope (VLT). These counts extend to $\sim 60''$ and to a limiting magnitude of $m_K \approx 17$. Down to the magnitude limit ($K = 15.5$) of the BSE09 sample, the ISAAC counts are $\sim 80\%$ complete beyond $\sim 15''$.

Figure 1 includes number counts from all the stars in the ISAAC sample with $K \leqslant 15.5$, and within the region $20'' \leqslant R \leqslant 60''$. The observed positions were converted to projected densities using the kernel routine described in Schödel et al. (2007) including corrections for completeness and crowding, as discussed in that paper. Confidence intervals were derived via the bootstrap. The ISAAC counts are seen to match very well onto the BSE09 counts, without the necessity for any ad hoc adjustment of the normalizations.

At larger radii, out to $R \approx 10\,\mathrm{pc} \approx 200''$, a number of studies have found $n \sim r^{-1.8}$ for the distribution of stellar light (Becklin & Neugebauer 1968; Haller et al. 1996; Genzel et al. 2000; Schödel et al. 2007). In all of what follows, we assume an asymptotic slope $d \log n / d \log r = -1.8$.

This leads us to parameterize the space density of the old stellar population as a power law with an inner core:

$$n(r) = n_0 \left(\frac{r}{r_0}\right)^{-\gamma_i} \left[1 + \left(\frac{r}{r_0}\right)^{\alpha}\right]^{(\gamma_i - \gamma)/\alpha} \quad (1)$$

with $\gamma = 1.8$. The parameter α controls the sharpness of the transition from outer to inner slopes. This model was fit to the number counts after projecting it onto the plane of the sky; in this way one avoids fitting a model to the surface density that does not correspond to a physical space density.

As is often found when modeling the luminosity profiles of cored elliptical galaxies (e.g., Terzić & Graham 2005), large values of α gave the best fits. The thick curve in Figure 1 shows the best-fit model when $\alpha = 4$; it has

$$n_0 = 0.21\mathrm{pc}^{-3}, \quad r_0 = 5''.5 = 0.21\ \mathrm{pc}, \quad \gamma_i = -1.0. \quad (2)$$

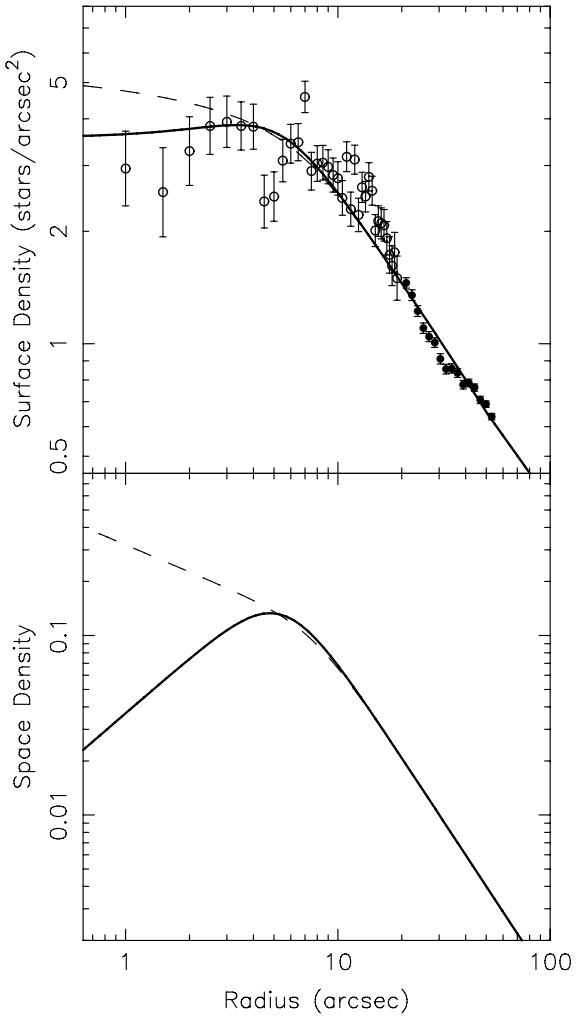

Figure 1. Upper panel: azimuthally averaged surface density of late-type stars at the Galactic center. Open circles are number counts of the "quality 1" late-type stars brighter than $K = 15.5$ in the sample of Buchholz et al. (2009; their Figure 11). Filled circles are derived from a kernel estimate of the projected density of all stars with $K \leqslant 15.5$ and $R \geqslant 20''$ in the sample of Schödel et al. (2007), after corrections for crowding and completeness. Curves show fits of the projected, parametric model, Equation (1), to the number-count data. Heavy curve is the best fit when the inner power-law slope is unconstrained; dashed curve shows the best fit when the inner slope is set at -0.5, the shallowest profile consistent with an isotropic velocity distribution. Both fits assume $\alpha = 4$ and $\gamma = 1.8$. Lower panel: space density profiles corresponding to the projected profiles in the upper panel.

The negative value of γ_i implies a space density that *decreases* toward the center (lower panel of Figure 1)—a central "hole."

Fits of this model to the data were found never to be terribly good ($\tilde{\chi}^2 \gtrsim 17$). There is a broad local maximum in the number counts at $R \approx 15''$ which would require additional parameters to fit. (In the two-dimensional counts, Figure 13 of BSE09, this overdensity is seen to be roughly symmetric about the origin.) The central minimum in the projected density is also difficult to reproduce.

Figure 2 shows the distribution of inner slopes γ_i obtained from the fits to 10^4 Monte Carlo samples bootstrapped from the number-count data in Figure 1. Ninety percent of the values fall in the range

$$-3.5 \leqslant \gamma_i \leqslant 0.82. \quad (3)$$

Negative values of γ_i (corresponding to centrally decreasing densities) are clearly preferred, though positive values are also acceptable.

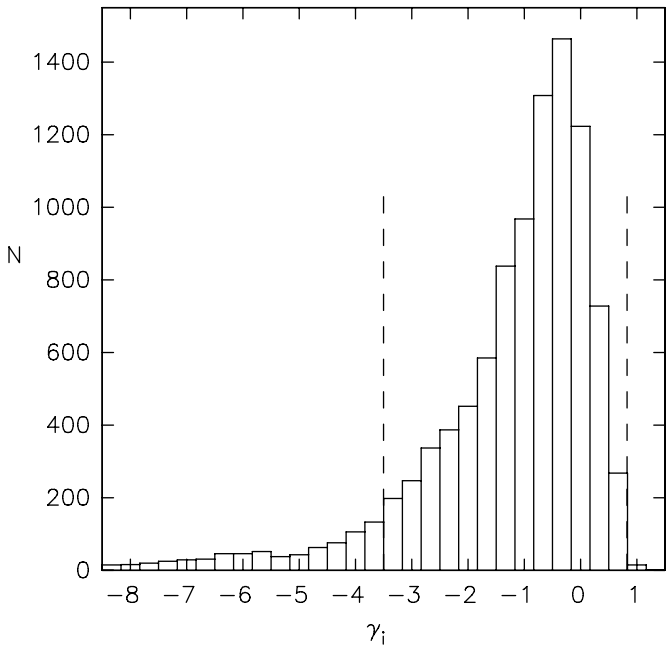

Figure 2. Distribution of inner slopes from fits to 10^4 Monte Carlo samples bootstrapped from the number-count data in Figure 1. Dashed lines delineate a 90% confidence interval.

If the stellar velocity distribution is isotropic, the space density *must* increase at least as fast as $r^{-0.5}$ near the SMBH (Section 3). The dotted curve in Figure 1 shows the best fit when γ_i is fixed at 1/2. The other parameters are

$$n_0 = 0.12\ \mathrm{pc}^{-3},\quad r_0 = 7\farcs7 = 0.30\ \mathrm{pc}. \tag{4}$$

This model can be (crudely) thought of having the minimum central density consistent with an isotropic velocity distribution. This fit is only slightly worse in a χ^2 sense (19.0 versus 17.5) than the fit with unconstrained inner slope, although it implies a very different *space* density profile inside ∼0.5 pc (Figure 1, lower panel).

A standard definition of the core radius is the projected radius where the surface density falls to 1/2 of its central value (e.g., King 1962). As a practical definition of the "central density," we take the value at $1'' \approx 0.04$ pc projected radius. Based on this definition, the core radius of the unconstrained fit in Figure 1 is

$$r_{\mathrm{core}} \approx 15\farcs2 \approx 0.59\ \mathrm{pc} \tag{5}$$

and the core radius of the constrained fit ($\gamma_i = -1/2$) is

$$r_{\mathrm{core}} \approx 10\farcs8 \approx 0.42\ \mathrm{pc}. \tag{6}$$

Thus, the core radius of the Milky Way nuclear star cluster (NSC) is ∼0.5 pc.

2.2. Relaxation Time

The relatively low central density of stars implied by Figure 1 and the apparently non-relaxed form of $n(r)$ are suggestive of a long two-body relaxation time. Spitzer (1987) defines the local relaxation time as

$$t_r = \frac{0.33\sigma^3}{G^2 n m^2 \ln\Lambda} \tag{7}$$

$$= 1.2\times 10^9\ \mathrm{yr}\frac{[\sigma(\mathrm{km\ s^{-1}})]^3}{\rho(\,M_\odot\,\mathrm{pc}^{-3})[m/\,M_\odot][\ln\Lambda/15]}, \tag{8}$$

where σ is the rms velocity in any direction, ρ is the stellar mass density, m is the mass of one star, and $\ln\Lambda$ is the Coulomb logarithm. This expression assumes that all stars have the same mass and that their velocity distribution is isotropic (Maxwellian).

To apply Equation (8), we need an estimate of $\rho(r)$. Dynamical estimates of ρ are to be preferred, given the large systematic uncertainties associated with converting a luminosity density into a mass density near the Galactic center (Schödel et al. 2007; Buchholz et al. 2009).

Inside ∼1 pc, the best dynamical constraints on ρ come from the recent proper-motion study of Schödel et al. (2009). These authors detected, for the first time, an unambiguous signature of the gravitational force from the distributed mass on the stellar motions, in the region 0.25 pc $\lesssim r \lesssim$ 1 pc; inside this region the gravitational force from the SMBH cannot be disentangled from that of the stars. Schödel et al. inferred a distributed mass of $\sim(1\pm0.5)\times10^6\ M_\odot$ in a sphere of radius 1 pc around SgrA*. The functional form of $\rho(r)$ was not well constrained, although the formal best fits were obtained with models in which the mass density decreased toward the center.

We use the Schödel et al. results to normalize the density of our "isotropic" $n(r)$, Equations (1) and (4). Defining

$$\tilde{M}_\star \equiv \frac{M_\star(r\leqslant 1\ \mathrm{pc})}{10^6\ M_\odot} \approx 1, \tag{9}$$

the mass density becomes

$$\rho(r) = 9.9\times10^5\ M_\odot\,\mathrm{pc}^{-3}\tilde{M}_\star\xi^{-0.5}(1+\xi^4)^{-0.325} \tag{10}$$

with $\xi = r/0.30$ pc. We then calculate the (isotropic) velocity dispersion from the Jeans equation,

$$\rho(r)\sigma(r)^2 = G\int_r^\infty dr' r'^{-2}[M_\bullet + M_\star(<r')]\rho(r'). \tag{11}$$

Figure 3 shows the resulting $t_r(r)$ assuming $\ln\Lambda = 15$, $m = M_\odot$, and three values of $\tilde{M}_\star$.

The Schödel et al. (2009) proper-motion data do not constrain the density beyond ∼1 pc. In this region, we assume

$$\rho(r) = 10^5\tilde{\rho}\left(\frac{r}{1\ \mathrm{pc}}\right)^{-1.8} M_\odot\,\mathrm{pc}^{-3}, \tag{12}$$

a simple continuation of the model fit at smaller radii. Below we argue for a "preferred" density model with $\tilde{\rho} = 1.5$, but in Figure 3 we allow the normalization:

$$\tilde{\rho} \equiv \frac{\rho(1\ \mathrm{pc})}{10^5\ M_\odot} \tag{13}$$

to have the values $\tilde{\rho} = (0.75, 1.5, 3)$. The Jeans equation was again used to compute $\sigma(r)$. The resulting $t_r(r)$ curves match well onto the curves at smaller radii and there is little dependence of t_r on $\tilde{\rho}$ within this radial range.

Also shown in Figure 3 is the influence radius r_{infl} of the SMBH, defined as the root of the equation

$$\sigma^2(x) = \frac{GM_\bullet}{x}. \tag{14}$$

Using the preferred density model with $\tilde{\rho} = 1.5$, one finds $r_{\mathrm{infl}} \approx 2.5$ pc. The relaxation time at $r \approx r_{\mathrm{infl}}$ is a reasonable estimate of the timescale over which gravitational encounters

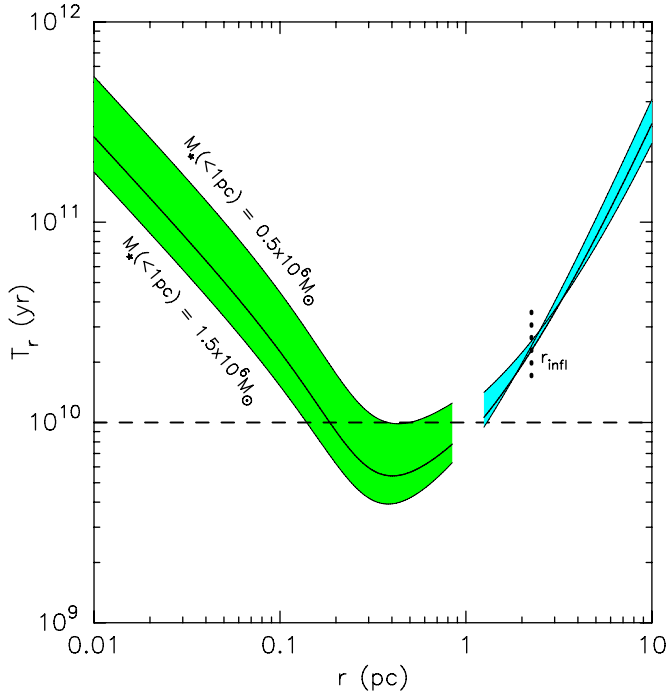

Figure 3. Relaxation time vs. radius at the Galactic center. Curves on the left (green filled region) assume the mass density of Equation (10) with three normalizations, such that the total (distributed) mass within 1 pc is $\tilde{M}_\star \equiv M_\star(<1\mathrm{pc})/M_\odot = (0.5, 1.0, 1.5)\times10^6$; the $\tilde{M}_\star = 1.0\times10^6$ model is shown as the heavy line. Curves on the right (blue filled region) assume $\rho \propto r^{-1.8}$ at all radii with various values for the normalizing density at 1 pc, $\rho_0 = (0.75, 1.5, 3)\times10^5\,M_\odot\,\mathrm{pc}^{-3}$; the $\rho_0 = 1.5\times10^5\,M_\odot\,\mathrm{pc}^{-3}$ (preferred) model is shown with the heavy line. Vertical tick mark is the SMBH influence radius computed using $\sigma(r)$ from the preferred model.

(A color version of this figure is available in the online journal.)

can change the gross properties of the core. Figure 3 shows that the relaxation time at r_{infl} is $\gtrsim$(2–3) $\times\,10^{10}$ yr.

The estimates of t_r in Figure 3 assume a single population of 1 $M_\odot$ stars. In reality, the Galactic center contains a range of mass groups, each of which might have a different velocity distribution. Given the relatively long relaxation time, a natural case to consider is a distribution of stellar masses, all of which have the same velocity dispersion at every radius. Equation (8) becomes in this case

$$t_r = \frac{0.33\sigma^3}{\rho\tilde{m}G\ln\Lambda}, \tag{15a}$$

$$\tilde{m} = \frac{\int N(m)m^2dm}{\int N(m)mdm}, \tag{15b}$$

and $N(m)dm$ is the number of stars with masses in the range m to m+dm (e.g., Merritt 2004). Since Equation (8) was derived from the diffusion coefficient $\langle(\Delta v_\parallel)^2\rangle$ describing gravitational scattering, Equation (15a) is properly interpreted as the time for a test star's velocity to be randomized by encounters with more massive objects. Making standard assumptions about the IMF gives $\tilde{m} \approx 1\,M_\odot$ (Merritt 2004); if the density is dominated locally by stellar BHs then $\tilde{m} \approx m_{\mathrm{BH}} \approx 10\,M_\odot$. It has been argued that $\tilde{m}$ may be even larger outside the central few parsecs due to giant molecular clouds (Perets et al. 2007).

3. MAKING A CORE

The classical model for a core (e.g., Tremaine 1997) is a region of constant gravitational potential ϕ and constant phase-space density f near the center of a galaxy. If the central potential is dominated by an SMBH, $\phi(r) \approx -GM_\bullet/r$ and a constant f translates into a steeply rising ρ:

$$\rho = \int f d^3\mathbf{v} \propto f\int_0^{\sqrt{-2\phi(r)}} v^2dv \propto f(-2\phi)^{3/2} \propto r^{-3/2} \tag{16}$$

inside $\sim r_{\mathrm{infl}}$ (Peebles 1972), inconsistent with the observed distribution.

The Galactic center has a core of size ~0.5 pc, smaller than $r_{\mathrm{infl}} \approx 2.5$ pc (Figures 1 and 3) so Equation (16) would apply in this region. Making a core similar to the observed core therefore requires a reduction in the value of f on orbits that pass inside ~0.5 pc.

There are of course many ways to do this. Given that the number counts do not strongly constrain the form of $n(r)$ within the core (Figure 2), we choose not to solve the inverse problem $n \rightarrow f$. Instead, we focus on two simple core models, both motivated by physical arguments, that are consistent with the number-count data.

The starting point is a power-law density of stars at all radii around the SMBH, $\rho_i \propto r^{-\gamma}$, $0 \leqslant r \leqslant \infty$. For definiteness, we normalize the density of this initial (i.e., coreless) model to be

$$\rho_i(r) = 1.5\times10^5\left(\frac{r}{1\ \mathrm{pc}}\right)^{-1.8} M_\odot\,\mathrm{pc}^{-3} \tag{17}$$

and we assume $n_i(r) \propto \rho_i(r)$. (The latter assumption will be relaxed in Section 5.) Equation (17) is just Equation (12) with $\tilde{\rho} = 1.5$. The normalizing constant is similar to what various authors have derived in the past for the mass density at 1 pc; e.g., $\tilde{\rho} \approx 1.8$ (Genzel et al. 2003), $\tilde{\rho} \approx 2.0$ (Schödel et al. 2007), etc. The exact normalization is not critical in what follows: it serves mostly to fix the relaxation time, and as Figure 3 shows, t_r in the region of interest is weakly dependent on the density normalization. We show below that our "preferred" value of $\tilde{\rho}$ gives a good fit to the observed stellar velocities at $r \approx r_{\mathrm{infl}}$.

The stellar mass implied by this model inside 1 pc is $\sim1.6\times10^6\,M_\odot$. This is the mass *before* the core has been carved out; for consistency, this mass should exceed the dynamically inferred (distributed) mass inside 1 pc, $\sim(1\pm0.5)\times10^6\,M_\odot$ (Schödel et al. 2009), and it does. At the same time, the proper-motion data are consistent with the mass implied by the unmodified power-law model, so we cannot robustly infer the presence of a core in the Galactic center *mass* distribution from the proper-motion data alone.

The gravitational potential generated by $\rho_i(r)$, including the contribution from the SMBH, can be written as

$$\phi(r) - \phi(r_0) = \frac{GM_\bullet}{r_0}\left(1 - \frac{r_o}{r}\right) \tag{18}$$

$$-\frac{1}{2-\gamma}\frac{GM_0}{r_0}\left[1 - \left(\frac{r}{r_0}\right)^{2-\gamma}\right], \tag{19}$$

where r_0 is a fiducial radius, taken in what follows to be 1 pc, $M_0 = 10^6\tilde{M}_\star\,M_\odot$ is the distributed mass inside r_0, and $\gamma = 1.8$. The isotropic distribution function $f_i(E)$ corresponding to the pair of functions (ρ_i, ϕ) can be derived numerically from the Eddington (1916) formula:

$$f_i(E) = \frac{1}{m}\frac{1}{\sqrt{8}\pi^2}\frac{d}{dE}\int_{\phi(r)}^{E}\frac{d\rho_i}{d\phi}\frac{d\phi}{\sqrt{E-\phi}}, \tag{20}$$

where $E = v^2/2 + \phi(r)$ is the energy per unit mass of a star. (Note that the subscript i refers here to "initial," not "isotropic.") Isotropy is a reasonable assumption, although as we will show, some reasonable models for a core imply substantial anisotropy.

3.1. Core Origins

Before proceeding, we consider possible mechanisms for the formation of a parsec-scale core at the center of a galaxy like the Milky Way.

1. *A binary SMBH.* In giant elliptical galaxies, cores are often attributed to ejection of stars by a pre-existing binary SMBH (Faber et al. 1997; Milosavljević & Merritt 2001), and possibly to gravitational-wave recoil after binary coalescence (Boylan-Kolchin et al. 2004; Gualandris & Merritt 2008). This model naturally explains the sizes of many observed cores—comparable to the influence radius of the (single) observed SMBH—if it is assumed that the galaxy grew through at least one "major merger," with comparably massive SMBHs (Merritt 2006a). However, the binary SMBH model seems less relevant to a disk-dominated system like the Milky Way, which may never have experienced a major merger. Based on a standard ΛCDM cosmological model, the probability that the Milky Way has avoided accreting a galaxy with halo mass 1/4 that of the Milky Way or greater, since a redshift of $z = 2$, is ∼30% (Merritt et al. 2002). The most recent major merger is likely to have occurred 10–12 Gyr ago, around the time of formation of the thick disk (Wyse 2001).
2. *Inspiral of multiple, smaller BHs.* A single intermediate-mass black hole (IMBH) of mass $\sim 10^4\,M_\odot$, spiralling in against a pre-existing stellar density cusp, creates a core of radius ∼0.05–0.1 pc (Baumgardt et al. 2006). Repeated inspiral events could create a larger core, although the displaced mass would increase at a less than linear rate with the number of inspirals. Nevertheless, some models postulate one such event every $\sim 10^7$ yr (Portegies Zwart et al. 2006); if so, more than one IMBH would probably be present at any given time in the inner parsec.
3. *An enlarged loss cone.* Gravitational encounters drive a mass flux of $\sim M_\bullet/t_r(r_{\rm infl})$ into Sgr A*. The core that results from this diffusive loss process is very small: its size is comparable to the radius of the capture sphere—either the tidal disruption radius, $r_t \approx 10^{-5}$ pc, or the Schwarzschild radius, $r_{\rm Sch} \approx 10^{-6}$ pc. The core is small because the depleted orbits are continuously resupplied by diffusion from orbits of larger angular momentum and energy. If there were some way to transfer the mass in stars of $\sim M_\bullet$ into the SMBH on a timescale $\ll t_r$—say, a crossing time—the resulting core would be much larger. This could happen if the NSC were appreciably triaxial, even if only transiently, since many orbits near an SMBH in a triaxial cluster are "centrophilic," passing arbitrarily close to the SMBH after a finite time (some multiple of the crossing time; Poon & Merritt 2001). The size of the resultant core is determined by a number of factors, including the degree of non-axisymmetry and the population of the various orbit families, but it could be of order $\sim r_{\rm infl}$ (Merritt & Poon 2004).
4. *Localized star formation.* Stars might form only, or preferentially, beyond a certain radius from SgrA*, resulting in a low density inside this radius. This possibility is discussed in more detail in Section 6.1.
5. *Feedback in active nuclei* has also been proposed as a rapid core-formation mechanism (Peirani et al. 2008).

3.2. Isotropic Core

A simple way to lower the density of stars near the SMBH is to set

$$f(E) = 0, \quad E \leqslant E_b. \tag{21}$$

Such a truncation leaves the velocity distribution isotropic. The cutoff energy can be expressed in terms of a cutoff radius r_b where

$$E_b \approx \phi(r_b). \tag{22}$$

The configuration-space density after removal of the most-bound stars is

$$\rho(r) \approx \rho_i(r), \quad r \geqslant r_b \tag{23a}$$

$$\approx 4\sqrt{2}\pi \int_{\phi(r_b)}^{\infty} dE f_i(E)\sqrt{\phi(r) - E}, \quad r < r_b. \tag{23b}$$

The "approximately equal" sign in these expressions is due to the fact that removal of the most-bound stars causes a change in the gravitational potential. We ignore that complication in what follows, i.e., we replace "≈" by "=" in Equations (22) and (23) and similar expressions below. The resultant error in ρ is at most a few percent, since ϕ is dominated by the SMBH at $r \lesssim r_{\rm infl}$, and by the stellar potential due for $r \gtrsim r_{\rm infl}$.

At small radii, $r \ll r_b \lesssim r_{\rm infl}$, the density is

$$\rho \approx 4\sqrt{2}\pi\sqrt{-\phi(r)}\int_{\phi(r_b)}^{\infty} dE f_i(E) \propto r^{-1/2}. \tag{24}$$

In spite of the zero-density hole in phase space, the configuration-space density diverges, mildly, toward the SMBH. This demonstrates that an isotropic f is not consistent with a strictly flat core, much less with a central dip in ρ.

Figure 4 shows space and projected density profiles for various values of r_b. The observed number counts are reasonably well fit by a model with

$$r_b \approx 0.5 \text{ pc}. \tag{25}$$

This value of r_b is close to the core radius derived above from the number counts. In other words, in these simple core models, $r_b \approx r_{\rm core}$.

The strange character of these (idealized) models—a zero phase-space density and a nonzero configuration-space density—implies some other strange properties. In the Appendix, the distribution of orbital elements for stars passing near the SMBH is derived. In spite of the isotropic f, the orbits near the center are very eccentric, with an expected size $a \approx 0.2 r_b \approx 0.1$ pc.

3.3. Anisotropic Core

Figure 1 suggests that $n(r)$ may be decreasing toward SgrA*. As our second model, we create a core by removing all stars on orbits that pass within the sphere $r = r_b$ around the SMBH. Such a model is a crude description of what happens when a binary SMBH ejects stars: in this case, r_b would be approximately the binary semimajor axis. Collisional destruction of (all) stars that pass within a distance r_b of the SMBH would also result in such a truncation of f.

Since we are preferentially removing stars on low-angular-momentum orbits, the velocity distribution in the core will be anisotropic, biased toward circular motions.

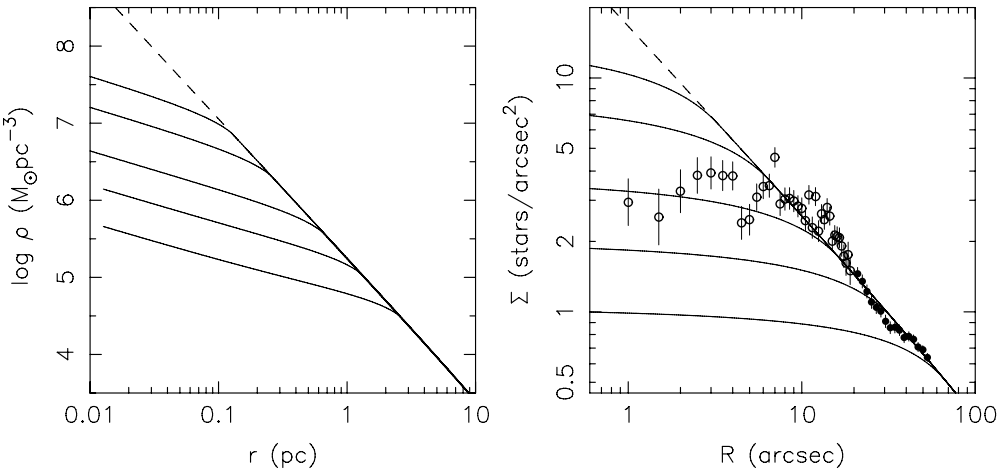

Figure 4. "Isotropic" core models, created by setting $f = 0$ at low (bound) energies, $E \leqslant E_b \equiv \phi(r_b)$, starting from a power-law model in the density, $\rho \propto r^{-1.8}$ (shown as the dashed line in both panels). Left panel shows space densities for $r_b = (0.1, 0.2, 0.5, 1, 2)$ pc. Right panel shows surface densities of the same models, compared to the number-count data from Figure 1. The vertical normalization of the models in this panel was chosen arbitrarily.

We define $E_b = \phi(r_b)$ as before, and E_c is the energy (kinetic plus potential) of a test particle on a circular orbit of radius r_b. If the core is small, $r_b \ll r_{\rm infl}$, then $E_c \approx E_b/2$. Starting again from a power-law density profile, Equation (17), and an isotropic distribution function, Equation (20), we now set $f = 0$ when either

$$E \leqslant E_c \tag{26a}$$

or

$$J^2 \leqslant J_b^2 = 2r_b^2(E - E_b); \tag{26b}$$

$J_b(E)$ is the specific angular momentum of an orbit with energy E and periapse r_b. The configuration-space density is now zero inside r_b:

$$\rho(r) = 0, \quad r \leqslant r_b. \tag{27}$$

Outside r_b, the density is lowered at *all* radii due to the absence of low-J stars:

$$\rho(r) = \frac{2\pi}{r^2}\int_{E_0(r)} dE f_i(E) \int_{J_b^2}^{2r^2(E-\phi(r))} \frac{dJ^2}{\sqrt{2\,[E-\phi(r)] - J^2/r^2}}$$
$$= 4\sqrt{2}\pi\left(1 - \frac{r_b^2}{r^2}\right)^{1/2} \int_{E_0(r)}^{\infty} dE f_i(E)\sqrt{E - E_0}. \tag{28}$$

Here,

$$E_0 = \frac{r^2\phi(r) - r_b^2 E_b}{r^2 - r_b^2} \tag{29}$$

is the minimum energy of orbits that pass through r without also passing below r_b.

Figure 5 shows density profiles for anisotropic-core models with various r_b. The observed number counts are reasonably well fit by a model with

$$r_b \approx 0.1\text{pc}. \tag{30}$$

Note that a given value of r_b produces a larger core than in the isotropic-core models, since a larger region of phase space is affected.

Defining σ_r and σ_t as the one-dimensional velocity dispersions in the radial and tangential directions, one finds

$$\rho\sigma_r^2 = \frac{8\sqrt{2}\pi}{3}\left(1 - \frac{r_b^2}{r^2}\right)^{3/2} \int_{E_0}^{\infty} dE f_i(E)(E - E_0)^{3/2}, \tag{31a}$$

$$\rho\sigma_t^2 = \rho\sigma_r^2 + 4\sqrt{2}\pi\frac{r_b^2}{r^2}\sqrt{1 - \frac{r_b^2}{r^2}}\int_{E_0}^{\infty} dE f_i(E)\sqrt{E - E_0}(E - E_b) \tag{31b}$$

for $r > r_b$; at smaller radii $\rho = 0$. The anisotropy, defined in the usual way as $\beta = 1 - \sigma_t^2/\sigma_r^2$, is then

$$\beta(r) = -\frac{3}{2}\frac{r_b^2}{r^2 - r_b^2}\frac{\int_{E_0}^{\infty} dE f_i(E)(E - E_b)\sqrt{E - E_0}}{\int_{E_0}^{\infty} dE f_i(E)(E - E_0)^{3/2}} \tag{32}$$

and is manifestly negative, i.e., $\sigma_t > \sigma_r$.

Figure 6 plots anisotropy profiles for the models in Figure 5 as well as projected velocity dispersion profiles in the plane of the sky, compared with the observed, proper-motion-based velocity dispersions from Schödel et al. (2009). The same values of r_b that give a good fit to the number-count data, also appear to fit the proper-motion data reasonably well. The tangential anisotropies predicted by these value of r_b—which peak between ∼2 and ∼5 arcsec—are consistent with what is observed, although the statistical error bars are so large that no clear discrimination between theoretical models can be made.

This figure also shows that the adopted density normalization, Equation (17), yields velocities that are consistent with the proper-motion data.

4. EVOLUTIONARY MODELS

The distributions of stars illustrated in Figure 1, and in the simple phase-space models of Figures 4 and 5, are different from the collisionally relaxed distributions normally associated with stars around an SMBH (Bahcall & Wolf 1976; Bahcall & Wolf 1977). This may be a consequence of the relatively long relaxation time at the Galactic center (Figure 3). A key question is whether models with a core can survive on Gyr timescales. In order to investigate this question, in this section we consider time-dependent models for the phase-space distribution, starting from initial conditions like those discussed in Section 3.

Models that are initially isotropic will remain close to isotropy as they evolve. Given such initial conditions, the isotropic,

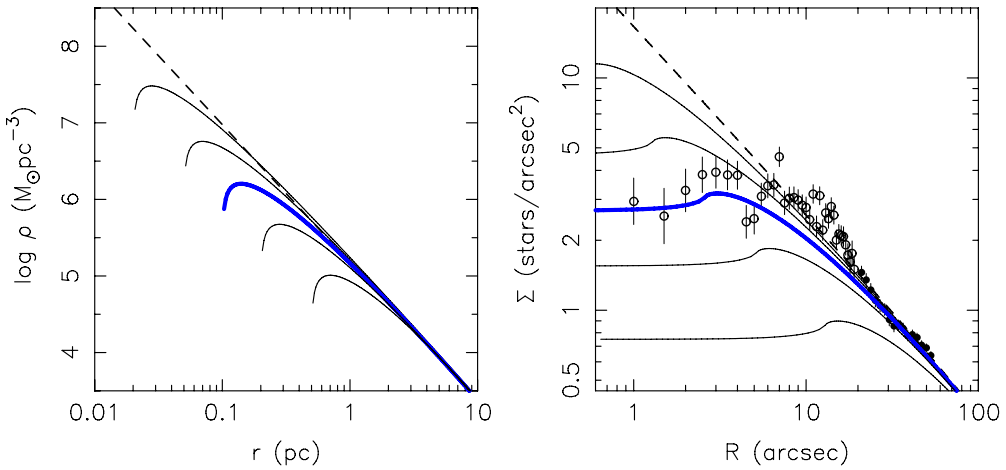

Figure 5. "Anisotropic" core models, created by setting $f = 0$ on orbits that pass below r_b. Left panel shows space densities for $r_b = (0.02, 0.05, 0.1, 0.2, 0.5)$ pc. Right panel shows surface densities of the same models, compared to the number-count data from Figure 1. Blue (thick) curve is marked for comparison with the same model in Figure 6. The vertical normalization of the models in the right panel was chosen arbitrarily.

(A color version of this figure is available in the online journal.)

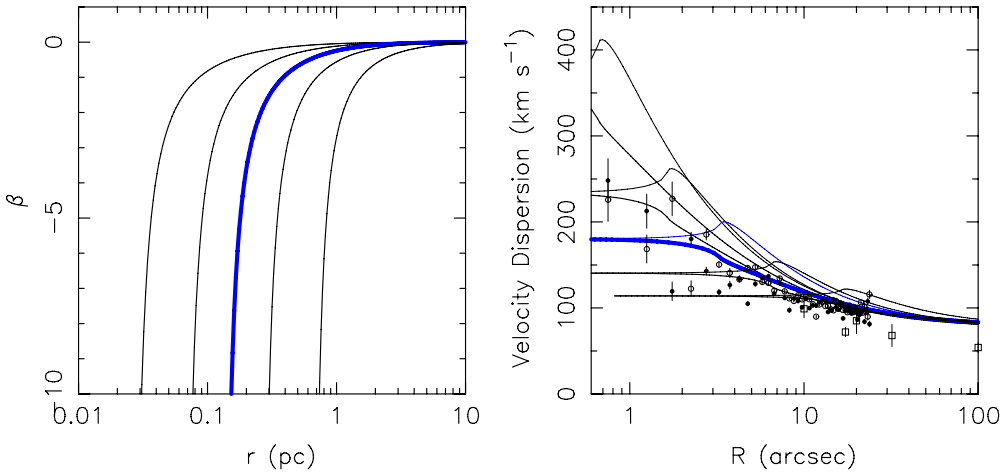

Figure 6. Kinematics of the models of Figure 5. Left panel: anisotropy profiles. Right panel: projected, radial (thick lines) and tangential (thin lines) velocity dispersions in the plane of the sky, compared with the observed σ_R (filled circles) and σ_T (open circles) from Schödel et al. (2009).

(A color version of this figure is available in the online journal.)

orbit-averaged Fokker–Planck equation (Hénon 1961) should provide a good description of the evolution.

Initially anisotropic models will evolve both in J- and E-space. Here, we make the approximation that the evolution can be divided into two sequential phases: "fast" evolution in J, on a timescale $\ll t_r$, followed by "slow" evolution in E, on a timescale $\sim t_r$. The justification follows from an argument made originally by Frank & Rees (1976): diffusion of stars into a point-mass "sink" is dominated by scattering of low-J orbits, on a timescale

$$t_\theta \approx \theta(r)^2 t_r(r), \tag{33}$$

where $\theta \approx (r_b/r)^{1/2}$ is the angle within which a star's velocity vector must lie in order for its orbit to intersect the central sink—in our case, the edge of the low-density core at $r \approx r_b$. The square-root dependence of θ on t_θ reflects the fact that evolution in J is a diffusive process. Thus,

$$t_\theta \approx \frac{r_b}{r} t_r \tag{34}$$

implying the separation of timescales for stars at $r \gtrsim r_b$.

In addition to being physically motivated, this approximation allows us to treat the evolution in J and E via differential equations with just one space dimension, and to formally separate the "isotropization time" from the timescale for changes in the radial (i.e., energy) distribution.

The separation of timescales breaks down for certain orbits, e.g., the lowest-energy orbits with $E \lesssim E_b$, and a full, $f(E, J, t)$ treatment could certainly be justified. Here, we note only that our initial conditions are somewhat arbitrary, and that changes in the E-dependence of f that would otherwise occur during the "fast" evolutionary phase could be seen as establishing a slightly different $f(E)$ at the start of the "slow" evolutionary phase.

As the phase-space density evolves, the configuration-space density $\rho(r)$ also changes, as well as the velocity dispersions $\sigma_r(r)$, $\sigma_t(r)$. Our main constraint on these models is that the distribution of stars, after $\sim$10 Gyr, be consistent with the observed distribution of late-type stars at the Galactic center. It is also reasonable to require that a model which matches the data now, not be in such a rapid state of evolution that it would quickly (in a time $\ll$10 Gyr) evolve to a very different form.

4.1. Evolution in J

4.1.1. Equations

The orbit-averaged Fokker–Planck equation describing changes in f due to diffusion in J-space is (e.g., Cohn 1979)

$$\frac{\partial N}{\partial t} = \frac{\partial}{\partial \mathcal{R}}\left(D_{\mathcal{R}} f + D_{\mathcal{R}R}\frac{\partial f}{\partial \mathcal{R}}\right). \tag{35}$$

Here, $\mathcal{R} = J^2/J_c^2$ is a scaled angular momentum variable, $J_c(E)$ is the angular momentum of a circular orbit of energy E, $N(E,\mathcal{R}) = 4\pi^2 P(E,\mathcal{R}) J_c^2(E) f(E,\mathcal{R})$ is the number density of stars in $(E,\mathcal{R})$ space, $P(E,\mathcal{R})$ is the radial period of an orbit, and $\{D_{\mathcal{R}}, D_{\mathcal{R}R}\}$ are the angular momentum diffusion coefficients:

$$D_{\mathcal{R}}(E,\mathcal{R}) = -16\pi^2 \mathcal{R} r_c^2(E)\int \frac{dr}{v_r}\left(1-\frac{v_c^2}{v^2}\right) F_1(E,r), \tag{36a}$$

$$D_{\mathcal{R}R}(E,\mathcal{R}) = \frac{16\pi^2}{3}\mathcal{R}\int\frac{dr}{v_r}\left\{2\frac{r^2}{v^2}\left[v_t^2\left(\frac{v^2}{v_c^2}-1\right)^2 + v_r^2\right]F_0(E) + 3\frac{r^2 v_r^2}{v^2}F_1(E,r) + \frac{r^2}{v^2}\left[2v_t^2\left(\frac{v^2}{v_c^2}-1\right)^2 - v_r^2\right]F_2(E,r)\right\}, \tag{36b}$$

with

$$F_0(E) = 4\pi\Gamma\int_E^\infty dE'\overline{f}(E'), \tag{37a}$$

$$F_1(E,r) = 4\pi\Gamma\int_{\phi(r)}^E dE'\overline{f}(E')\left(\frac{E'-\phi}{E-\phi}\right)^{1/2}, \tag{37b}$$

$$F_2(E,r) = 4\pi\Gamma\int_{\phi(r)}^E dE'\overline{f}(E')\left(\frac{E'-\phi}{E-\phi}\right)^{3/2} \tag{37c}$$

and $\Gamma \equiv 4\pi G^2 m^2 \ln\Lambda$. In the expressions (36), the integration interval is the radial range from periapsis to apoapsis. Definitions for subsidiary variables can be found in Cohn (1979) whose notation is adopted here. Following Shapiro & Marchant (1978) and Cohn & Kulsrud (1978), the angular-momentum-averaged phase-space density $\overline{f}$ that appears in Equations (37) is defined as

$$\overline{f}(E) = \int_0^1 d\mathcal{R} f(E,\mathcal{R}). \tag{38}$$

Because we are ignoring changes in E, the function $\overline{f}(E)$ does not change with time, nor do the diffusion coefficients $\{D_{\mathcal{R}}, D_{\mathcal{R}R}\}$.

The practice of some authors (e.g., Milosavljević & Merritt 2003) of approximating the $\mathcal{R}$-diffusion coefficients by their limiting values as $\mathcal{R}\to 0$ is not followed here.

Equation (35) was advanced in time numerically using the NAG routine `d03pcf`. Initial conditions were $f(E,J)$ corresponding to the anisotropic-core models described in the previous section, with various values of r_b (e.g., Figures 5 and 6).

Scaling of the Fokker–Planck models to physical units of length and mass is fixed by the power-law density model, Equation (17), used to generate the initial conditions. Since the Fokker–Planck equations are orbit averaged, the relevant time unit is the relaxation time. In what follows, times will be expressed in years, based on a scaling that assumes a relaxation time given by Equation (15a) with $\tilde{m} = 1\,M_\odot$ and $\ln\Lambda = 15$. If $\tilde{m}$ and $\ln\Lambda$ have different values than these. The times given below should be multiplied by

$$\left(\frac{\tilde{m}}{1\,M_\odot}\right)^{-1}\left(\frac{\ln\Lambda}{15}\right)^{-1}. \tag{39}$$

4.1.2. Results

Figure 7 shows the evolution of the space and projected densities for the anisotropic-core model with $r_b = 0.1$ pc (blue curves in Figures 5 and 6). The central configuration-space "hole" is rapidly filled as the low-angular-momentum orbits are repopulated; by a time of $\sim 10^9$ yr, the central density is essentially unchanging inside $\sim r_b$. Because (by assumption) there is no diffusion in E, the central hole in *phase* space remains, and so $\rho(r)$ evolves asymptotically to the $\sim r^{-1/2}$ form demanded by an isotropic $f(E)$ with a low-energy truncation (Figure 4). The surface density evolves much less, since even at the (projected) center, the surface density is dominated by stars in the power-law envelope. Thus, this model is a reasonable fit to the observed number counts either at $t = 0$ or at later times: the refilling of the low-J orbits does not greatly affect the observed densities.

Figure 8 illustrates the evolution toward isotropy in the same time integration. Initially, there is a strong velocity anisotropy near the center due to the lack of eccentric orbits (Figure 6). However, the refilling of the low-J orbits increases σ_r at $r \lesssim r_b$ on a timescale of $\sim$1 Gyr and the core is essentially isotropic thereafter.

Proper-motion data from the (projected) inner parsec of the Milky Way indicate a slight degree of anisotropy (Schödel et al. 2009). We define an averaged anisotropy parameter $\langle\mathcal{B}\rangle$ as

$$\langle\mathcal{B}\rangle \equiv 1 - \frac{\langle\sigma_T^2\rangle}{\langle\sigma_R^2\rangle}, \tag{40}$$

where σ_R and σ_T are the radial and tangential velocity dispersions in the plane of the sky and the $\langle\rangle$ denote number-weighted averages over some radial range. Adopting $1'' \leqslant R \leqslant 10''$ for this range, the late-type stars near the Galactic center have

$$\langle\mathcal{B}\rangle = -0.124^{0.098}_{-1.05}, \tag{41}$$

where the (90%) confidence intervals were derived via the bootstrap. Figure 9 compares the observed value of $\langle\mathcal{B}\rangle$ with the values predicted by the evolving models. The 90% observed upper bound, $\langle\mathcal{B}\rangle \approx -0.026$, is almost consistent with isotropy, which is the asymptotic state of the time-dependent models; while the observed lower bound, $\langle\mathcal{B}\rangle \approx -0.23$, is almost as low as the initial anisotropy of the most extreme core model considered here. Thus, the Fokker–Planck models remain consistent with the observed degree of anisotropy over essentially the entire time interval and for a wide range of initial conditions.

Figure 9 also gives an indication of how the time to establish isotropy in an initially anisotropic core varies with the size of the core. Larger values of r_b imply both a higher initial anisotropy, and a longer timescale for the establishment of isotropy.

4.1.3. Summary

Cores formed by the exclusion of small-periapse orbits evolve toward isotropy on a ~Gyr timescale. This evolution does not

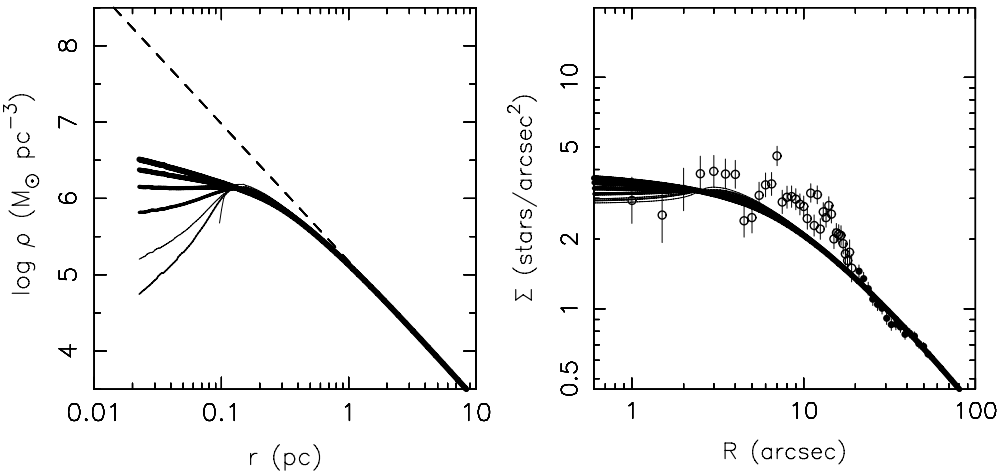

Figure 7. Evolution of the density of the "anisotropic-core" model with $r_b = 0.1$ pc due to diffusion in J. Curves show space (left) and projected (right) densities at times $(0, 0.1, 0.2, 0.5, 1, 2, 5) \times 10^9$ yr. Line thickness increases with time. Other symbols are as in Figure 5.

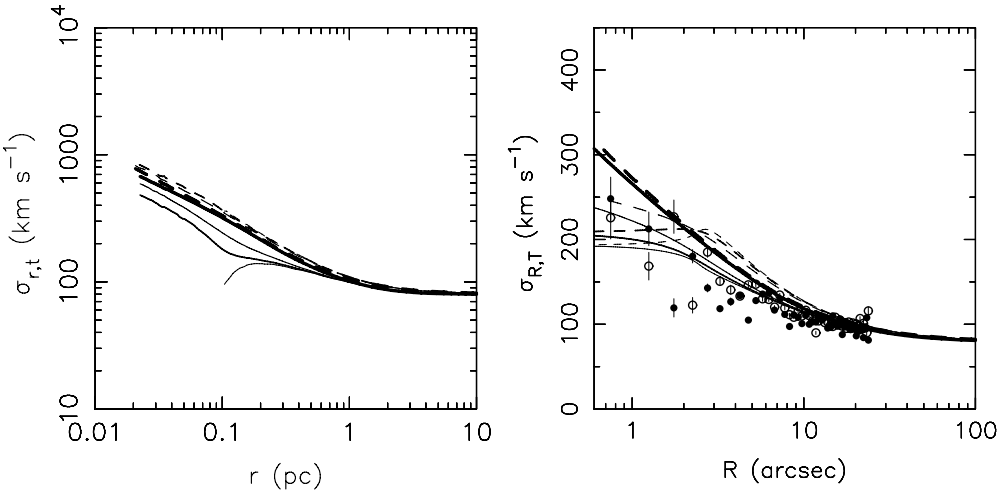

Figure 8. Evolution of the space (left) and projected (right) velocity dispersions for the same "anisotropic-core" model illustrated in Figure 7. Solid (dashed) curves are radial (tangential) velocity dispersions. Line thickness increases with time; $t = (0, 0.1, 0.5, 5) \times 10^9$ yr. Symbols have same meaning as in Figure 6.

produce great changes in the observable properties of the core, either in the density or the velocity dispersions. The anisotropy observed at the Galactic center is consistent with the evolving models at both early and late times.

4.2. Evolution in E

Evolution in E-space drives f toward the quasi-steady-state form

$$f \sim |E|^{1/4}, \quad \rho \sim r^{-7/4} \tag{42}$$

at $E \lesssim -GM_\bullet/r_{\rm infl}$ and $r \lesssim r_{\rm infl}$, on a timescale that is roughly the relaxation time at $r_{\rm infl}$ (Bahcall & Wolf 1976; Lightman & Shapiro 1977). Equation (42) corresponds to a zero net flux in E-space near the hole. In reality, loss of stars into the SMBH implies a nonzero flux, causing a gradual evolution (expansion) of the cluster, although without much change in the form of $\rho(r)$ (e.g., Shapiro & Marchant 1978; Murphy et al. 1991). We ignore that complication here since the density in our models near the SMBH remains far below that of the quasi-steady-state models at most times, implying a very small flux into the SMBH.

Many authors have explored quasi-steady-state solutions to this equation and to the more general equations that allow for a dependence of f on orbital angular momentum and stellar mass (as reviewed by Merritt 2006b). After a *finite* time $\lesssim t_r$, the form of $f(E)$ will still reflect the initial conditions. Quinlan (1996) emphasized this in the case of stellar systems without central SMBHs. Freitag et al. (2006a) explored in a limited way how the structure of Galactic center models depends on the assumed initial density profile. They considered initial profiles $\rho \sim r^{-\gamma}$ with γ as small as 0.75 (steeper, i.e., closer to the asymptotic Bahcall–Wolf form, than the steepest initial profiles considered here). Freitag et al. found that a time of order $t_r(r_{\rm infl})$ is required to erase details of the initial conditions. Based on Figure 3 that time is ∼20 Gyr.

4.2.1. Equations

The orbit-averaged, isotropic Fokker–Planck equation is

$$\frac{\partial N}{\partial t} = \frac{\partial}{\partial E}\left(D_{\rm EE}\frac{\partial f}{\partial E} + D_E f\right), \tag{43a}$$

$$D_{\rm EE}(E) = 16\pi^3\Gamma \times \left[q(E)\int_{-\infty}^{E} dE' f(E') + \int_E^{\infty} dE' q(E') f(E')\right], \tag{43b}$$

$$D_E(E) = 16\pi^3\Gamma \int_E^{\infty} dE' p(E') f(E') \tag{43c}$$

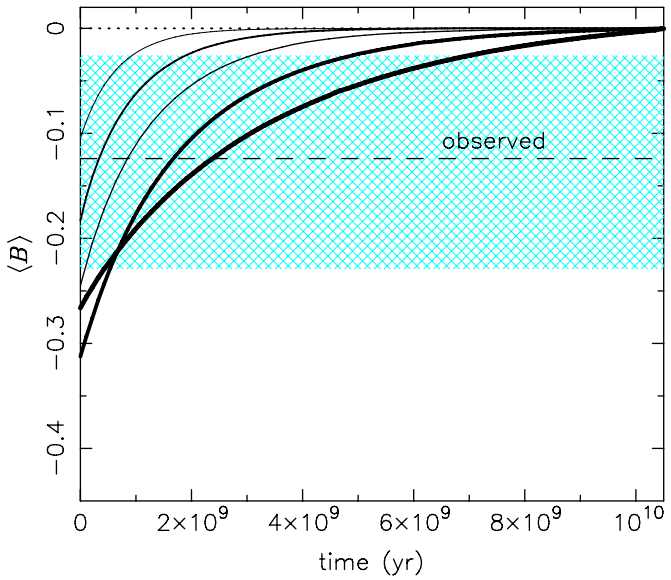

Figure 9. Evolution of the projected anisotropy parameter $\langle \mathcal{B} \rangle$ defined in the text, computed over the projected annulus $1'' \leqslant R \leqslant 10''$. Curves are from integrations starting from the five initial models illustrated in Figures 5 and 6; increasing line thickness denotes increasing values of r_b, the initial truncation radius, from 0.02 pc to 0.5 pc. Dashed line is the anisotropy at the Galactic center as computed from the proper-motion data of Schödel et al. (2009), with the 90% confidence interval shown as the hatched (blue) region.

(A color version of this figure is available in the online journal.)

(e.g., Cohn 1980; Spitzer 1987). Here, $N(E) = 4\pi^2 p(E)$ is the number density of stars in energy space and $p(E) = 4\sqrt{2}\int r^2\sqrt{E-\phi(r)}dr = \partial q/\partial E$ is a phase-space volume element. The functions f, D_E, and $D_{\rm EE}$ are understood to depend on time; as above, the gravitational potential is assumed to remain fixed, as do the functions p and q.

Equations (43) were solved using the NAG routine `d03pcf`. The E-space flux was set to zero at the inner boundary of the energy grid, as justified above. Two sorts of initial conditions were considered: (1) $f(E)$ corresponding to an "isotropic-core" model and (2) $\mathcal{R}$-averaged f's from the final time steps of the J-integrations described in the previous section, which started from "anisotropic-core" models. (The final f's from these integrations were almost precisely isotropic; cf. Figure 9.) In both cases, the initial conditions will be labeled in terms of r_b.

4.2.2. Results

Figure 10 shows the evolution of the "isotropic-core" model with $r_b = 1$ pc. Diffusion in E-space causes stars to gradually occupy orbits of lower (more bound) energies. However, even after 10 Gyr—roughly the relaxation time at r_b (Figure 3)—f and ρ are still far from their steady-state forms at low energies/small radii. The Bahcall–Wolf solution is only reached after a time that is roughly twice as long.

The lower panel of Figure 10 highlights an interesting coincidence. All of the models considered here have (by assumption) a density that obeys

$$\rho \sim r^{-1.8} \tag{44}$$

at large radii—the observed dependence of the density of old stars on radius beyond ∼1 pc. But this is essentially the same slope as in the steady-state Bahcall–Wolf profile, $\rho \sim r^{-1.75}$ which is the asymptotic form of $\rho(r)$ at *small* radii. As long as the initial core radius is smaller than $\sim r_{\rm infl}$, it follows that

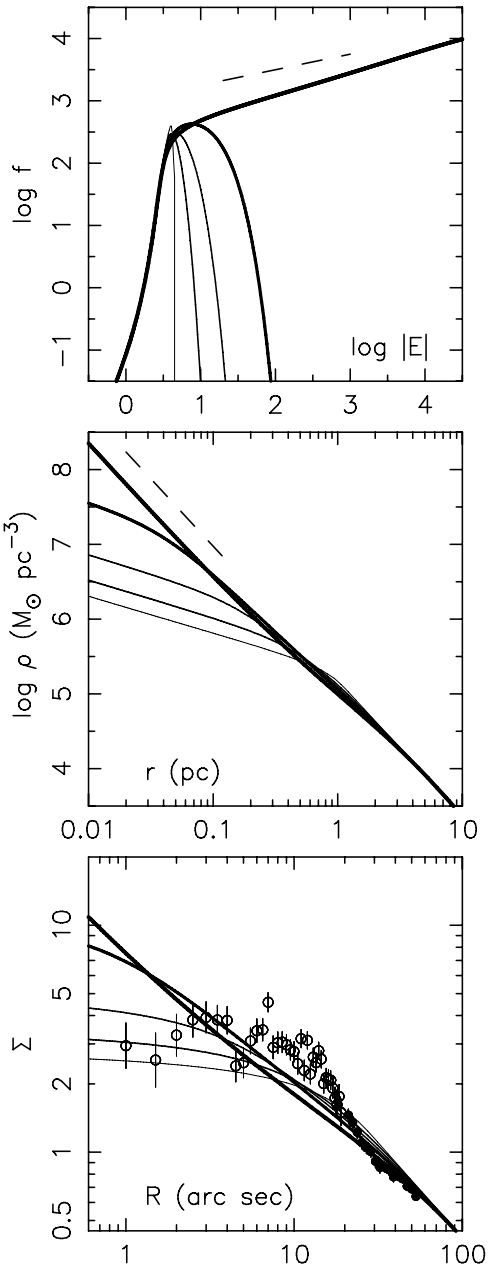

Figure 10. Evolution of the phase-space density (top), configuration-space density (middle), and surface density (bottom) of the "isotropic-core" model with $r_b = 1$ pc (Figure 4). Increasing line thickness denotes increasing time, $t = (0, 0.2, 0.5, 1, 2) \times 10^{10}$ yr. Dashed lines are the asymptotic forms for f and ρ, i.e., $f \sim |E|^{1/4}$, $\rho \sim r^{-7/4}$. E, f, and Σ are in arbitrary units.

$\rho(r)$ will evolve in an approximately self-similar way: the core will shrink, while outside the core, $\rho(r)$ will continue to obey $\rho \sim r^{-1.8}$. Reproducing the observed density profile is therefore simply a matter of choosing the appropriate, initial value of r_b.

Which values of r_b give cores of the right size now? Two estimates were derived in Section 2 for the core radius of the old stellar population, 0.59 and 0.42 pc. These values are plotted in Figure 11, which also shows core radii as a function of time in the evolving models (computed in the same way, i.e., by finding the projected radius at which the surface density falls to 1/2 of its value at 0.04 pc). The figure suggests that the currently observed core is consistent with initial cores having sizes in the range

$$1\ {\rm pc} \lesssim r_{\rm core} \lesssim 1.5\ {\rm pc}, \tag{45}$$

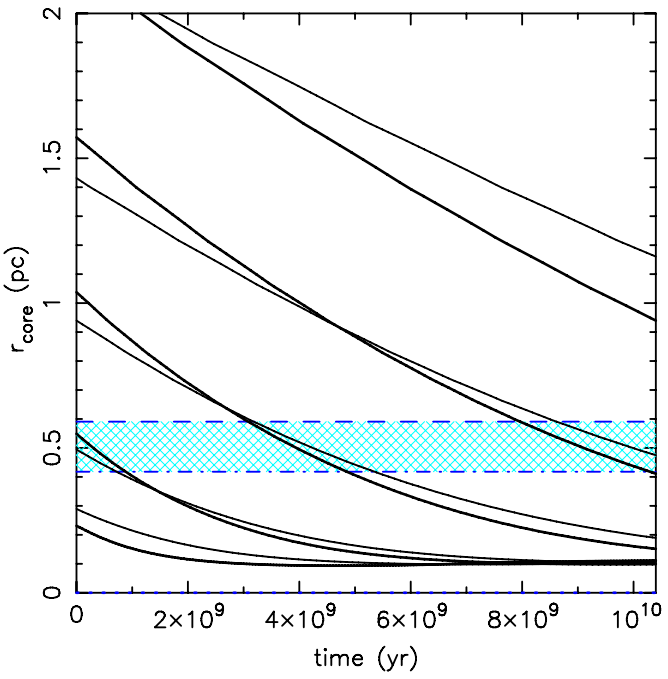

Figure 11. Evolution of the core radius in various models. Thick curves: "isotropic-core" models. Thin curves: "anisotropic-core" models. The hatched (blue) region encloses the two estimates of the Milky Way core radius, as discussed in the text.

(A color version of this figure is available in the online journal.)

or 2–3 times the current value. These values are comparable with the SMBH influence radius (Figure 3).

5. SEGREGATION OF THE MASSIVE REMNANTS

Old stellar populations contain remnants: white dwarves (WDs), neutron stars (NSs), and stellar-mass BHs, the end products of stars with initial masses 1–8 $M_\odot$ (WDs), 8–30 $M_\odot$ (NSs), and ∼30–100 $M_\odot$ (BHs). Standard assumptions about the IMF imply that ∼1% of the total mass of an old population should be in the form of stellar BHs (Alexander 2005), although observational constraints on the BH number density near the Galactic center are weak (e.g., Muno et al. 2005).

The stellar BHs have significantly higher masses (∼×10) than either the main-sequence stars or the other types of remnant that collectively dominate the total mass density. The BHs should therefore lose orbital energy due to dynamical friction and congregate around the SMBH. Assuming that the total density obeys an expression similar to Equation (17), i.e., $\rho \sim r^{-2}$, the time for a 10 $M_\odot$ BH on a circular orbit to spiral all the way in to the center is less than 10 Gyr for a starting radius inside 4–5 pc (Morris 1993; Miralda-Escudé & Gould 2000). Depending on the assumed mass fraction in BHs, and on their initial density profile, the mass density of BHs after 5–10 Gyr is predicted to match or exceed that of the other populations inside $\sim 10^{-2}$ pc. If this occurs, the BHs will undergo gravitational scattering from themselves and from the other populations, leading to a quasi-steady-state $n \sim r^{-2}$ density profile in the innermost regions, and to a slightly shallower profile in the lighter mass components (Freitag et al. 2006a; Hopman & Alexander 2006a; Alexander & Hopman 2009).

All of the studies cited above assumed or derived a total mass density that increases as $\rho \sim r^{-\gamma}$, $1.3 \lesssim \gamma \lesssim 2.3$ down to $\sim 10^{-5}$ pc from the SMBH. If instead the dominant population has a core, the dynamical friction force will increase more slowly toward the center inside $\sim r_{\rm core}$, implying somewhat longer inspiral times.

But there is potentially an even more dramatic way in which a core can affect the rate of orbital decay, as we now show. The instantaneous frictional force felt by a (massive) test body of mass $m_{\rm BH}$ and velocity $\mathbf{v}$ is

$$\mathbf{a} = -\frac{4\pi G^2 m_{\rm BH}\rho(r)F(v)\ln\Lambda}{v^3}\mathbf{v}, \tag{46}$$

where $F(v)$ is the fraction of stars locally that are moving more slowly than v. If the latter are described by an isotropic f, then

$$\rho(r)F(v) = 4\sqrt{2}\pi\int_{\phi(r)}^{v^2/2+\phi(r)} dE f(E)\sqrt{E-\phi(r)}. \tag{47}$$

If in addition f is truncated at energies below E_b—an "isotropic core"—then F falls to zero for orbits with energies

$$\frac{v^2}{2} + \phi(r) \leqslant E_b \tag{48}$$

since there are *no* stars locally that move slower than v for these energies—even if the configuration-space density is nonzero. Assuming a circular orbit for the test body, and that the orbit lies inside the influence radius of the SMBH, this condition becomes

$$r \lesssim \frac{r_b}{2} \tag{49}$$

with $E_b = \phi(r_b)$. Thus, inside ∼1/2 the core radius, the frictional force drops precisely to zero.

This result is not simply an artifact of the brute-force truncation of f. Consider a core in which $\rho \propto r^{-\gamma}$. In a point-mass potential, this density is reproduced by

$$f(E) = f_0|E|^{\gamma-3/2} \tag{50}$$

and F for a circular orbit is easily shown to be

$$F(\gamma) = \frac{2}{\sqrt{\pi}}\frac{\Gamma(\gamma+1)}{\Gamma(\gamma-1/2)}\int_{1/2}^{1} dz z^{\gamma-3/2}\sqrt{1-z}. \tag{51}$$

This function varies smoothly from $F = 0.5$ at $\gamma = 2$, the singular isothermal sphere, to $F = 0$ at $\gamma = 0.5$.

As an even more general illustration of this effect, we computed the evolution of a circular orbit in a background density described by the broken power-law model of Equation (1) with $\alpha = 2$. The outer slope was fixed at $\gamma = 1.8$ and the normalization was chosen to reproduce the density of the "fiducial" model, Equation (17), outside the core. Setting the inner slope γ_i to 1.8 gives a model similar to those assumed in the studies cited above; while small values of γ_i correspond to a core. The radius r of a test body's orbit decays as

$$\frac{1}{r}\frac{dr}{dt} = -|\mathbf{a}|\left(\frac{dJ}{dr}\right)^{-1}. \tag{52}$$

The function $F(v)$ was computed using the expression (Szell et al. 2005)

$$F(v) = 1 - \frac{1}{\rho}\int_E^0 d\phi'\frac{d\rho}{d\phi'} \times\left\{1+\frac{2}{\pi}\left[\frac{v/\sqrt{2}}{\sqrt{\phi'-E}} - \tan^{-1}\left(\frac{v/\sqrt{2}}{\sqrt{\phi'-E}}\right)\right]\right\}. \tag{53}$$

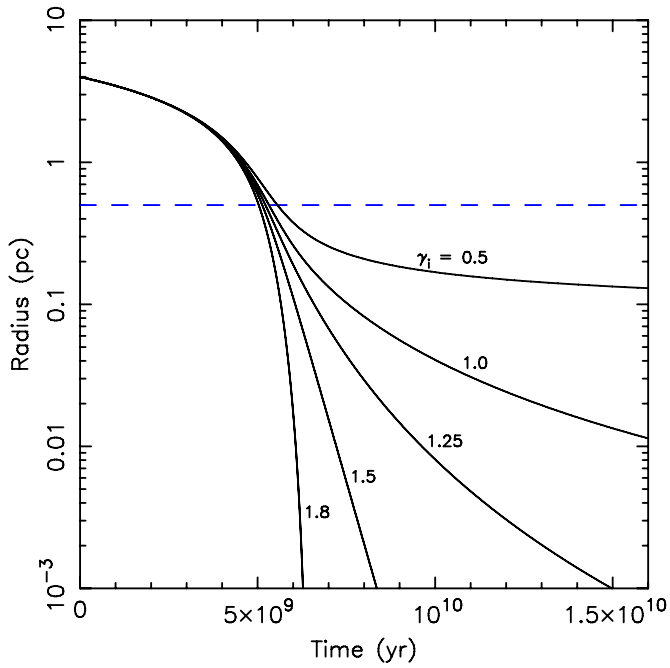

Figure 12. Trajectories of 10 $M_\odot$ BHs as they spiral in to the Galactic center on circular orbits, starting from a radius of 4 pc. The assumed background density is a power law, $\rho \propto r^{-1.8}$ at large radii, with an inner core of radius r_0, as described by Equation (1) with $\alpha = 2$; r_0 was set to 0.5 pc (dashed/blue line) and the inner power-law slope of the density was varied, as indicated.

(A color version of this figure is available in the online journal.)

Figure 12 shows the trajectories of 10 $M_\odot$ BHs starting from a distance of 4 pc, assuming various values for the inner density slope; in each case we set the core radius parameter r_0 to 0.5 pc. As predicted, the rate of orbital decay begins to slow when $r \lesssim r_0$ for small values of γ_i, and the decay essentially stalls, at $r \lesssim r_0/2$ pc, when $\gamma_i = 0.5$. We stress that the configuration-space density is nonzero at all radii in these models, and in fact increases monotonically toward the center; the precipitous drop in the frictional force is due to the lack of low-velocity stars in the core when γ_i is small.

Another consequence of a core is that the dynamical friction force along an orbit is not so strongly peaked near periapse, which is a necessary condition for an orbit to circularize. In the presence of a core, the distribution of BH orbits will therefore remain more nearly isotropic (assuming that it starts out isotropic). This, combined with the cutoff in the dynamical friction force at $r \approx r_0$, suggests that the evolved BH density would rise rapidly toward $r \approx r_0$, then follow $\sim r^{-0.5}$ toward smaller radii, the density law of an isotropic population with an inner hole in phase space. If the background density is itself evolving, as in the models of the previous section, the core radius of the population that produces the dynamical friction force will decrease with time, causing the radius of peak BH density to also migrate inward on the same timescale.

5.1. Equations

As in previous sections, the evolution of the distribution of stellar BHs was followed using the orbit-averaged Fokker–Planck equation. Define $f_{\rm BH}(E, \mathcal{R})$ to be the number density in phase space of a population of massive objects (BHs), of individual mass $m_{\rm BH}$. We assume that the associated mass density $\rho_{\rm BH}$ is small compared with the total mass density ρ due to stars and (less massive) remnants. Alexander & Hopman (2009) show that the limiting density ratio for ignoring the self-interaction of the BHs is $\rho_{\rm BH}/\rho_\star < m_\star/m_{\rm BH} \approx 0.1$. This condition is violated at late times in some of the integrations described below; this effectively defines the maximum time at which the solutions are valid.

The orbit-averaged equation describing the evolution of $f_{\rm BH}$ as the massive objects experience dynamical friction against the background of less massive objects is

$$\frac{\partial N_M}{\partial t} = \frac{\partial}{\partial E}\left(D_E f_{\rm BH}\right) + \frac{\partial}{\partial \mathcal{R}}\left(D_{\mathcal{R}} f_{\rm BH}\right), \tag{54}$$

where $N_M(E, \mathcal{R}) = 4\pi^2 P(E, \mathcal{R}) J_c^2(E) f_{\rm BH}(E, \mathcal{R})$ is the number density in $(E, \mathcal{R})$ space as before. The diffusion coefficients depend on the (possibly time-dependent) distribution of low-mass objects. Let $f_i(E, \mathcal{R}, t)$ be the phase-space number density of stars with mass m_i, $m_i \ll m_{\rm BH}$. Then (e.g., Takahashi 1997)

$$D_E(E, \mathcal{R}) = -8\pi^2 m_{\rm BH} J_c^2(E) \sum_i m_i \int \frac{dr}{v_r} F_{1i}(E, r), \tag{55a}$$

$$D_{\mathcal{R}}(E, \mathcal{R}) = -16\pi^2 m_{\rm BH} \mathcal{R} r_c^2(E) \times \sum_i m_i \int \frac{dr}{v_r}\left(1 - \frac{v_c^2}{v^2}\right) F_{1i}(E, r), \tag{55b}$$

with

$$F_{1i}(E, r) = 4\pi\gamma \int_{\phi(r)}^{E} dE' \overline{f}_i(E', t)\left(\frac{E' - \phi}{E - \phi}\right)^{1/2} \tag{56}$$

and $\gamma \equiv 4\pi G^2 \ln\Lambda$; $\overline{f}_i$ is the angular-momentum-averaged f as defined above.

Defining the phase-space mass densities of BHs and the other populations (collectively referred to, henceforth, as "the stars"), respectively, as

$$g_{\rm BH} = m_{\rm BH} f_{\rm BH}, \quad g = \sum_i m_i f_i, \tag{57}$$

the evolution equation for the BHs can be written as

$$\begin{aligned}\frac{P J_c^2}{8\pi\gamma m_{\rm BH}} \frac{\partial g_{\rm BH}}{\partial t} &= -\frac{\partial}{\partial E}\left[g_{\rm BH} J_c^2 \int \frac{dr}{v_r} \int_{\phi(r)}^{E} dE' \overline{g}(E', t)\left(\frac{E' - \phi}{E - \phi}\right)^{1/2}\right] \\ &\quad - 2\frac{\partial}{\partial \mathcal{R}}\left[g_{\rm BH} \mathcal{R} r_c^2 \int \frac{dr}{v_r}\left(1 - \frac{v_c^2}{v^2}\right) \int_{\phi(r)}^{E} dE' \overline{g}(E', t)\left(\frac{E' - \phi}{E - \phi}\right)^{1/2}\right].\end{aligned} \tag{58}$$

This equation was integrated forward using an explicit scheme with second-order space derivatives and first-order time derivative. Two choices were considered for the stellar phase-space density g: (1) a time-independent model with an "anisotropic core" and (2) a time-dependent, isotropic model in which g evolves according to Equation (55). In both cases, the phase-space density of the BHs was assumed to be the same as that of the stars at $t = 0$.

If the mass density in stellar BHs becomes comparable to that of the stars at any radius, Equations (59) are no longer valid, since the BHs will begin to feel perturbations from each other and because the stellar distribution will be affected by heating

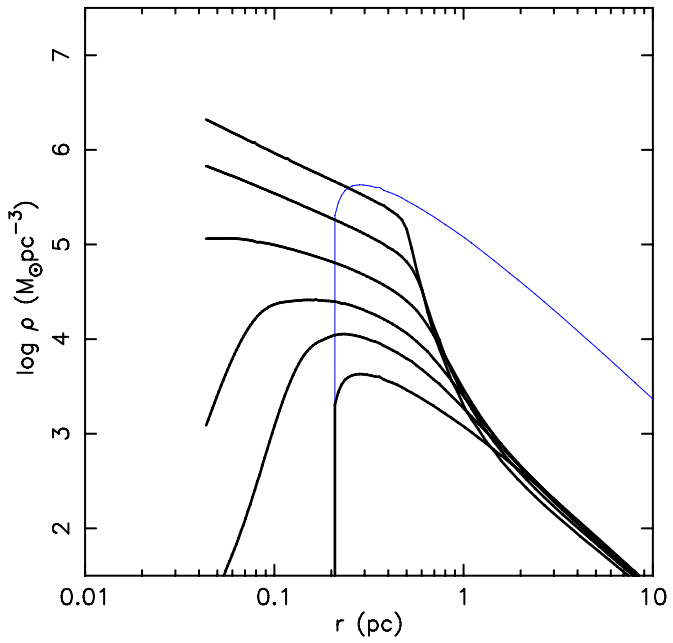

Figure 13. Evolution of the density of stellar BHs assuming a fixed background density, shown by the thin (blue) line. Curves show the density at times (0, 1, 2, 4, 8, 16) Gyr.

(A color version of this figure is available in the online journal.)

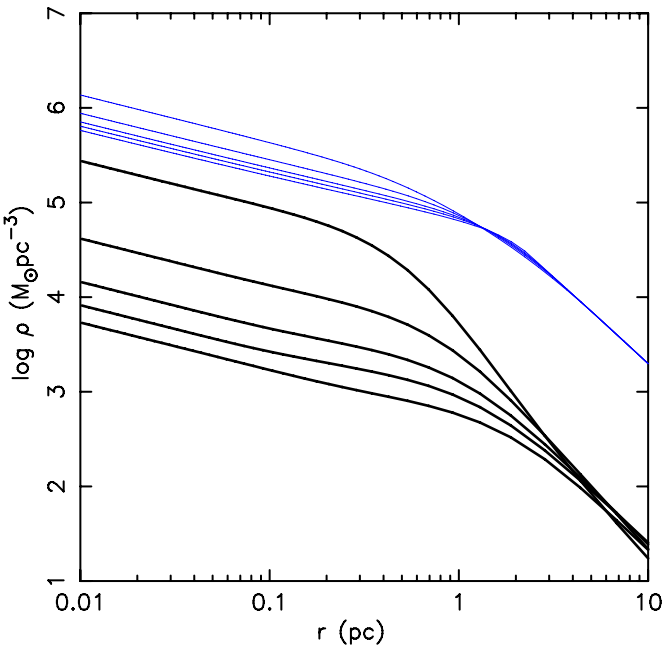

Figure 14. Evolution of the number density of stellar BHs (thick/black curves) assuming an evolving background (stellar) density (thin/blue curves), starting from an "isotropic-core" model with $r_b = 2$ pc in both components. Times shown are (0, 1, 2, 4, 8) Gyr.

(A color version of this figure is available in the online journal.)

from the BHs. Whether, or when, this occurs depends on the assumed initial normalization of $\rho_{\rm BH}$. In plots that follow, BHs were assumed to be a fraction 10^{-2} of the total mass density initially.

Results in this section are expressed in years, assuming that $m_{\rm BH} = 10\,M_\odot$. Times can be scaled to different values of $m_{\rm BH}$ using the simple proportionality of the dynamical friction force on $m_{\rm BH}$ (Equation (46)).

5.2. Results

Figure 13 shows the evolution of the BH mass density assuming a fixed stellar background, corresponding to an "anisotropic-core" model with $r_b = 0.2$ pc. The initial BH distribution is likewise anisotropic. As time progresses, the density of BHs drops at a radius of a few parsecs and rises inside $\sim$1 pc; BHs accumulate at energies near the core due to the falloff in the dynamical friction force there, as discussed above. At late times ($\gtrsim$5 Gyr), the BH velocity distribution is slightly biased toward circular motions beyond $\sim$1 pc, and toward radial motions inside $\sim$1 pc; as noted above, dynamical friction in the presence of a core does not efficiently circularize orbits. To a reasonable approximation, the phase-space distribution of the BHs at late times is isotropic, and because the *stellar* distribution has not been allowed to evolve, the BH density remains zero on orbits with energies below $E_c \approx E_b/2$. The result is a $\rho_{\rm BH} \sim r^{-0.5}$ cusp at $r \lesssim 2r_b \approx 0.4$ pc. Note that the density of BHs just approaches that of the stars at the final time (16 Gyr) in this integration.

Allowing the stellar distribution to evolve is more realistic. Figures 14 and 15 show the results of two such integrations. In Figure 14, the initial distributions of stars and BHs were generated from an "isotropic-core" model with $r_b = 2$ pc. The stellar distribution was allowed to evolve according to Equations (43), yielding a time-dependent $g(E, t)$ which was inserted into Equation (58) at each time step to compute the diffusion coefficients acting on $g_{\rm BH}$. In these integrations, the stellar core shrinks, on a timescale that is $\sim$10 times longer than the timescale for the BHs to accumulate around the core. As a result, the BHs "follow" the stellar core inward. Their density does not rise so steeply toward the core as in the integrations with fixed stellar density (Figure 13) since the radius at which they would otherwise accumulate changes with time. Figure 15 shows the mass enclosed within (0.1, 0.3, 1) pc versus time for both components, in a second integration starting from $r_b = 1$ pc. Also shown for comparison is the mass in BHs estimated by Miralda-Escudé & Gould (2000) to lie within the central parsec after 10 Gyr, assuming dynamical friction against a fixed stellar background, and the mass in BHs estimated by Hopman & Alexander (2006a) to lie within 0.1 pc, based on their steady-state multi-mass Fokker–Planck solutions.

The feature that we wish to emphasize here is the sensitivity, in our models, of the final density in BHs to the elapsed time. Figures 14 and 15 suggest that it would be unjustified to assume that the stellar BHs have reached a steady-state density by now at any radius inside $\sim$1 pc. This is even more true if star formation has been an ongoing process in the NSC (e.g., Serabyn & Morris 1996; Figer et al. 2004), since the mean age of stars and remnants may be much less than 10 Gyr (Section 6.1).

This point is made more forcefully in Figure 16, which compares stellar and BH densities at $r = 0.01$ pc in three models with different initial core sizes. The figure shows that when the evolving stellar core reaches a size consistent with the observed core, the density in stellar BHs can be substantially less than that of the stars at this radius. In the steady-state models, the BH density meets or exceeds that of the stars at radii of 10^{-2} to 10^{-1} pc (e.g., Freitag et al. 2006a, Figure 10), and gravitational-wave inspiral of BHs is dominated by BHs at these distances (Hils & Bender 1995; Hopman & Alexander 2005). The much lower densities found here have potentially important implications for the predicted rate of inspiral events, as discussed in more detail in Section 6.4.

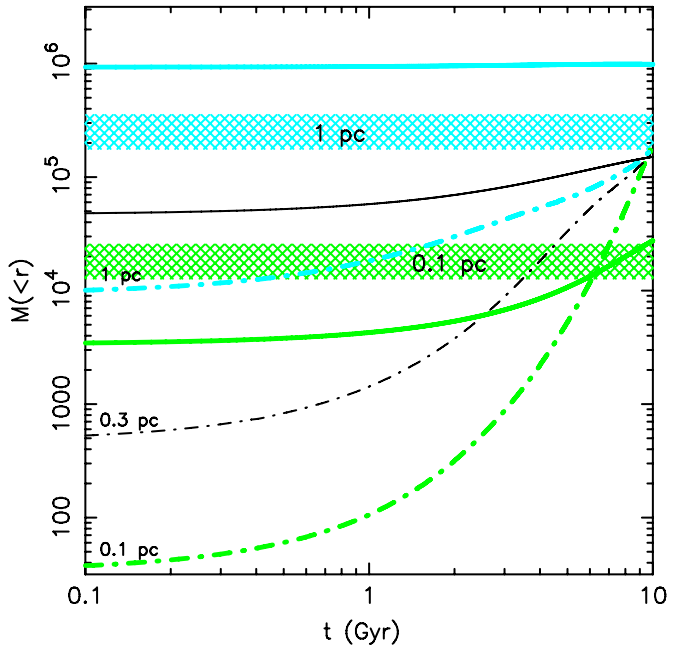

Figure 15. Evolution of the enclosed mass in stellar BHs (dash-dotted lines) and stars (solid lines) in an integration like that of Figure 14, with $r_b = 0.1$ pc. Curves show mass enclosed within (0.1, 0.3, 1.0) pc assuming that stellar BHs have initially 1% the mass density of stars at each radius. The hatched regions show the estimates of Miralda-Escudé & Gould (2000) for the mass of stellar BHs within 1 pc after 10 Gyr, assuming dynamical friction against a fixed stellar density cusp, and of Hopman & Alexander (2006a) for the mass of BHs within 0.1 pc based on steady-state Fokker–Planck solutions. The vertical width of each hatched region corresponds to an (arbitrary) factor 2 in mass.

(A color version of this figure is available in the online journal.)

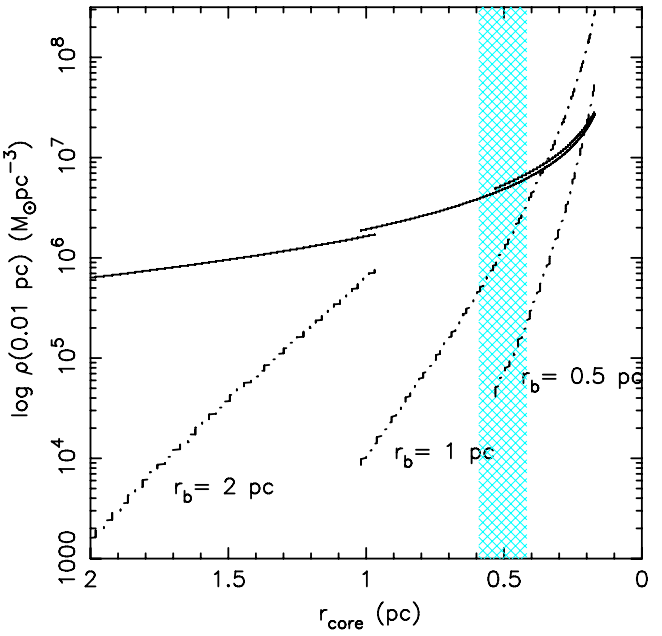

Figure 16. Density of stellar BHs (dash-dotted curves) and stars (solid curves) at $r = 0.01$ pc in three models with cores of different initial size, $r_b = (0.5, 1, 2)$ pc. Horizontal axis is core radius of the stars, which decreases with time as the core shrinks. Integration times are 10 Gyr. Vertical hatched region indicates the radius of the observed core.

(A color version of this figure is available in the online journal.)

In models with initial core radii $\lesssim$1.5 pc (small enough to reproduce the currently observed core), the density of stellar BHs after 10 Gyr becomes large enough that self-interactions between the BHs would be significant. A high enough density of BHs would also tend to accelerate the relaxation of the stellar component. While beyond the scope of this paper, tests of these predictions could be carried out via two-component, $f(E, L, t)$ models or N-body integrations.

5.2.1. Summary

The timescale for inspiral of 10 $M_\odot$ BHs to the center of the Galaxy is longer in models with a core than in models with a cusp, both because of the lower density of stars in the core, but also because the dynamical friction force drops essentially to zero at energies near the phase-space truncation energy that defines the core. Assuming that the BHs and the stars have the same distributions initially, the radius of peak density of the BHs tends to "follow" the stellar core as the latter shrinks. The density of BHs can remain substantially less than that of the stars at small radii ($r \lesssim$ 0.01–0.1 pc) even after the stellar core has shrunk to its observed size of ∼0.5 pc.

6. DISCUSSION

Topics discussed in this section include the dynamical consequences of ongoing star formation, predicted rates of stellar tidal disruptions and gravitational wave inspirals at the Galactic center, mechanisms for enhanced relaxation, the effect of a parsec-scale stellar core on inspiral of IMBHs, the rate of production of hypervelocity stars (HVSs) by collisions involving stellar BHs, and the connection between the core at the center of our Galaxy and the cores observed in other galaxies.

6.1. Star Formation

The Milky Way NSC sits at the center of a kiloparsec-scale Galactic bulge or bar which consists mainly of old (∼10 Gyr) evolved stars. On sub-kiloparsec scales, the Milky Way shows evidence for stellar populations with a range of ages. Serabyn & Morris (1996) argued that the conditions of the interstellar medium in the "Central Molecular Zone" would lead inexorably to inflow of molecular material and to continuous star formation activity in the central $\sim 10^2$ pc. Figer et al. (2004) modeled the luminosity function of stars in the inner ∼50 pc and argued that single-burst star formation models could be securely ruled out; they inferred a nearly constant rate of star formation rate over the last ∼10 Gyr. These and other studies (e.g., Mezger et al. 1999; Philipp et al. 1999) suggest that the NSC is not a simple inward extrapolation of the old bulge, but rather consists of an intermediate age population that has been undergoing continuous star formation since the creation of the Galaxy.

In a general way, continuous star formation strengthens the picture presented here of a nuclear cluster that is less than ∼1 relaxation time old, by reducing the mean age of stars from ∼10 Gyr to ∼5 Gyr.

Of more direct interest is the evidence for recent star formation in the inner ∼0.5 pc (Paumard 2008), the same region where the old stars exhibit a low-density core. The total mass of the young stars currently observed in this region is probably less than $10^4\ M_\odot$ (Figer 2008), making them dynamically insignificant. On the other hand, the starburst that created this population may have been just the most recent instance of an ongoing or episodic process. How would such a "source term" modify the evolutionary calculations presented above?

The answer clearly depends on the accumulated stellar mass and on the radial dependence of the star formation rate; both

are highly uncertain. Here, we limit ourselves to answering a simpler question: how would a population of stars, formed initially in a disk, evolve against the background of a pre-existing stellar core? We specifically ignore interactions between the disk stars, and assume that the background stars are fixed in their distribution. More detailed calculations, in which both populations are allowed to evolve, will be described in a subsequent paper (H. B. Perets et al. 2010, in preparation).

If the surface density of the young stellar disk is $\Sigma(r) \propto r^{-n}$, the distribution of orbital energies is $dN/dE = (dN/dr)(dr/dE) \propto |E|^{n-3}$. To simplify the evolutionary calculation, we suppose that the orbits of the young stars "randomize" in orientation and eccentricity on a timescale shorter than t_r. (Without trying to justify that assumption quantitatively, we note several mechanisms that might achieve this: standard relaxation as in Section 3, "resonant relaxation" as in Section 6.4, and torques from another disk or from a large-scale non-axisymmetric bulge component, etc.) The young stars can then be described by an isotropic f where $f(E, t = 0) \propto p(E)^{-1}N(E) \propto |E|^{n-1/2}$. The corresponding space density is $\rho(r, t = 0) \propto r^{-1-n}$. If the disk is truncated at an inner radius $r_{\rm in}$, then $\rho(r, t = 0) \propto r^{-1/2}$ inside $\sim r_{\rm in}$. We assume $n = 2$ and that the disk stars are initially distributed between 0.1 pc and 0.4 pc.

For the old stars, we assume a (fixed) $f_{\rm old}(E) = f_0|E|^A$, which corresponds to a density $\rho_{\rm old}(r) = \rho_0 r^{-\gamma}$, $\gamma = A + 3/2$, $r < r_{\rm infl}$. Substituting this expression for $f_{\rm old}$ into the energy-space diffusion coefficients D_E and $D_{\rm EE}$ of Equation (43) gives

$$D_E(E) = -\frac{32\sqrt{2}\pi^5}{3-2A} f_0 G^5 M_\bullet^3 m^2 \ln\Lambda |E|^{A-3/2}, \tag{59a}$$

$$D_{\rm EE}(E) = \frac{32\sqrt{2}\pi^5}{(1+A)(1-2A)} f_0 G^5 M_\bullet^3 m^2 \ln\Lambda |E|^{A-1/2} \tag{59b}$$

again assuming that the gravitational potential is due to the SMBH alone.

We adopt units for time and energy such that

$$4\pi\Gamma f_0 [T][E]^A = 1, \tag{60}$$

where $\Gamma \equiv 4\pi G^2 m^2 \ln\Lambda$. A natural energy unit is

$$[E] = \psi_0 \equiv \frac{GM_\bullet}{r_{\rm infl}}, \tag{61}$$

which makes the unit of time

$$[T]^{-1} = 16\pi^2 G^2 m^2 \ln\Lambda f_0 \psi_0^A. \tag{62}$$

In dimensionless variables, Equation (43) for the young stars then becomes

$$\frac{\partial f}{\partial t} = -E^{5/2}\frac{dF}{dE}, \tag{63a}$$

$$F(E) = -\frac{2}{(1+A)(1-2A)} E^C \frac{d}{dE}(E^B f), \tag{63b}$$

where

$$B = \frac{-(1+A)(1-2A)}{3-2A}, \quad C = \frac{-1+6A-8A^2}{2(3-2A)}. \tag{64}$$

The steady-state solution is given by setting $F(E) = 0$:

$$f(E, t \to \infty) \propto E^{-B}. \tag{65}$$

Choosing $A = 1/4$ ($\gamma = 7/4$) implies $B = -1/4$; in other words, test particles interacting with stars in a Bahcall–Wolf cusp evolve also to the Bahcall–Wolf form. However, other choices for A imply different steady-state solutions for the young stars.

Figure 17 shows time-dependent solutions to Equation (63) under two assumptions about the background population. In both cases, the (fixed) density of the old population was normalized to give a mass within 1 pc of $1.5 \times 10^6\, M_\odot$. Figure 17(a) assumes $\rho_{\rm old} \propto r^{-7/4}$ ($A = 1/4$), a Bahcall–Wolf cusp. In this case, the relaxation time at the initial disk radius is just a few Gyr, and the young stellar population also reaches a distribution close to the Bahcall–Wolf form after 5 Gyr, as expected. Gravitational encounters with the old stars tend to redistribute the young stars to both smaller and larger radii.

Figure 17(b) shows the case $\rho_{\rm old} \propto r^{-3/4}$ ($A = -3/4$), a lower-density core. Now, the relaxation time increases toward the center; the distribution of young stars hardly changes inside the original inner disk radius, and the net result of gravitational encounters is mostly to scatter the disk stars to larger radii. The steady-state form, $\rho \propto r^{-1.63}$, is only gradually approached, and only at radii outside the initial disk radius. There is essentially no evolution toward a Bahcall–Wolf cusp.

In both cases, the number of young stars that remain within the original outer disk radius after 5 Gyr is a small fraction of the initial number: $\sim 10^{-3}$ in the $A = 1/4$ case and ~ 0.15 for $A = -3/4$.

These results, while very preliminary, suggest that ongoing star formation need not greatly modify the conclusions that were arrived at above. As long as star formation occurs against the backdrop of a stellar core, the density profile of the young stars can remain relatively flat inside the initial disk radius. Their mean density is also strongly diluted by encounters with the older stars.

This conclusion may need to be modified in the case of the stellar remnants. The $\sim$10–100 very massive blue giant stars in the stellar disks will probably end their lives as an equal number of $10\, M_\odot$ BHs, with total mass $\sim 10^2$–$10^3\, M_\odot$. If such star forming events occur once per 10^8 yr, then $10^4\, M_\odot$–$10^5\, M_\odot$ in stellar BHs could accumulate in the central parsec over 10 Gyr.[1] The expected number of remnants will also depend strongly on the form of the IMF; for instance, a "top-heavy" IMF (Paumard et al. 2006) would produce many more stellar BHs per unit of total mass.

6.2. Rates of Tidal Disruption

The existence of a core implies a smaller rate of stellar tidal disruptions at the Galactic center than in models that assume a density cusp. The rate of scattering of stars into the SMBH's tidal disruption sphere, $r \leqslant r_t$, can be written as

$$\dot{N} = \int \mathcal{F}(E) dE, \tag{66}$$

where $\mathcal{F}(E)$ is the number of stars scattered per unit time and unit energy into r_t. In the models considered here, setting the core radius to zero gives $\rho \propto r^{-1.8}$ at all radii (Equation (12)), and this is also approximately the form of the density in the

[1] I thank Tal Alexander for pointing this out.

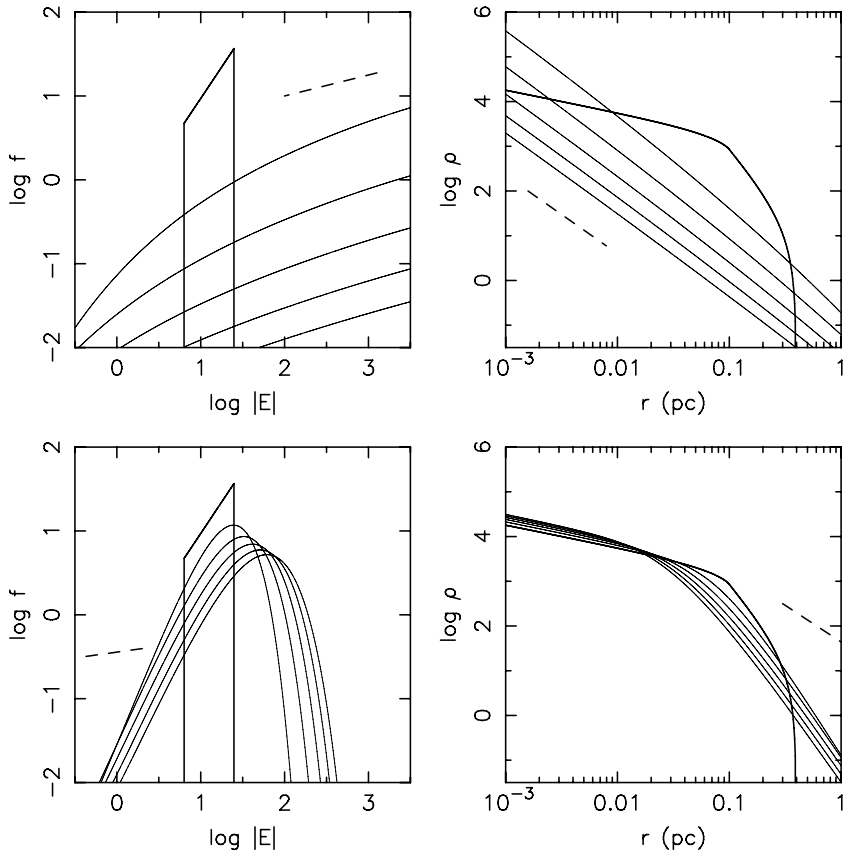

Figure 17. Evolution of $f(E,t)$ and $\rho(r,t)$ describing an isotropic population of "young" stars that formed initially in a disk, and subsequently scatter off of the "old" stars, assumed to have a fixed phase-space distribution. Initial conditions are shown in bold; subsequent times are $(1, 2, 3, 4, 5) \times 10^9$ yr, assuming that the mass in the old population within 1 pc is $1.5 \times 10^6\,M_\odot$. Length units were scaled to the Galactic center. (a) $f_{\rm old} \propto E^{0.25}$, $\rho_{\rm old} \propto r^{-7/4}$, the Bahcall–Wolf form. (b) $f_{\rm old} \propto E^{-3/4}$, $\rho_{\rm old} \propto r^{-3/4}$. Dashed lines show the steady-state slopes.

single-mass Bahcall–Wolf steady-state solution at $r \lesssim r_{\rm infl}$, $\rho \propto r^{-1.75}$. Both density laws, in turn, are close to a singular isothermal sphere, $\rho \propto r^{-2}$, for which the feeding rate has been shown to be

$$\dot{N} \approx 4.6 \times 10^{-4}\,{\rm yr}^{-1} \left(\frac{\sigma}{90\ {\rm km\ s}^{-1}}\right)^{7/2} \left(\frac{M_\bullet}{4 \times 10^6\,M_\odot}\right)^{-1} \quad (67)$$

assuming solar-type stars (Wang & Merritt 2004).

Carving out a core changes $\dot{N}$ for two reasons. (1) The energy integral, Equation (66), now has E_b as a lower limit rather than $-\infty$. (2) The diffusion coefficients $D_{\mathcal{R}}$, $D_{\mathcal{R}R}$ that determine the scattering rate at every E (Equations (36)) are smaller due again to the absence of stars with $E < E_b$.

A commonly made approximation (e.g., Cohn & Kulsrud 1978) is to ignore the contribution to $F(E)$ from scattering off of stars with energies that are smaller (i.e., more tightly bound) than E. In this approximation, the diffusion coefficients are not changed, at energies $E > E_b$, by the truncation of f at E_b, and the only change in $\dot{N}$ comes from the change in the lower integration limit for Equation (66).

Table 1 shows $\dot{N}$ for the Milky Way computed under this approximation, for various values of r_b, assuming an "isotropic core." (Recall that r_b is essentially equal to the core radius of the corresponding density profile, Figure 4, so that setting $r_b \approx 0.5$ pc gives a core of roughly the correct size for the Milky Way.) A 0.5 pc core implies a tidal flaring rate that is almost an order of magnitude smaller than for a coreless cusp.

Table 1
Stellar Tidal Disruption Rates

r_b (pc)	$\dot{N}$ (yr^{-1})
0	4.6×10^{-4}
0.1	2.7×10^{-4}
0.2	1.7×10^{-4}
0.5	5.6×10^{-5}
1	2.7×10^{-5}
2	2.0×10^{-5}

This conclusion should be considered extreme since it ignores changes in f that will necessarily tend to refill the depleted orbits over relaxation timescales. In principle, the time integrations of f in Section 4 could be used to compute the evolution of the tidal disruption rate. We postpone that calculation to a later paper, but make a related point here: if f is not in a steady state, the standard expressions for the flux into the loss cone (like the expressions that were used to derive Equation (67)) are not strictly valid (Milosavljević & Merritt 2003; Merritt & Wang 2005). This highlights the need to develop a more complete theory of time-dependent loss cones.

6.3. Enhanced Relaxation

The evolution equations for f and $f_{\rm BH}$ that were solved in Sections 4 and 5 were based on a standard, orbit-averaged Fokker–Planck treatment of gravitational encounters. The

results were scaled to physical time units assuming that relaxation is driven by perturbers with masses of roughly $M_\odot$.

Both of these assumptions have been questioned, in recent papers that argue for more efficient relaxation near the Galactic center (Hopman & Alexander 2006b; Perets et al. 2007). Two important points have been made: (1) the effectiveness of gravitational encounters at inducing changes in orbital angular momenta is increased for stars orbiting within the gravitational field of an SMBH, $r < r_{\rm infl}$, since the orbits are nearly Keplerian and they maintain their orientations for many radial periods, allowing torques to accumulate linearly with time ("resonant relaxation"; Rauch & Tremaine 1996). (2) If there is a distribution of masses in the scattering population, the effective relaxation time is determined by the second moment of the mass function (Equations (15)). The presence of even a small population of very massive objects ("massive perturbers") in the region of interest can reduce the effective relaxation time considerably.

We briefly discuss the applicability of these ideas to the evolutionary models discussed here.

Resonant relaxation. Resonant relaxation is relevant to the timescale for isotropization that was computed in Section 4. The resonant relaxation time is

$$t_{\rm RR} \approx \frac{1}{N(<a)}\left(\frac{M_\bullet}{m_\star}\right)^2 \frac{P^2(a)}{t_{\rm precess}} \tag{68}$$

(Hopman & Alexander 2006b) where $N(<a)$ is the number of perturbing stars, of mass $m_\star$, inside the orbit of the test star whose semimajor axis is a, P is the orbital period, and $t_{\rm precess}$ is the timescale above which orbits lose their coherence due to precession. If precession is due primarily to the gravitational force from the N stars, distributed spherically inside $r = a$, then

$$t_{\rm precess} \approx \frac{1}{N(<a)}\frac{M_\bullet}{m_\star}P(a) \tag{69}$$

and

$$t_{\rm RR} \approx \frac{M_\bullet}{m_\star}P(a) \tag{70a}$$

$$\approx 2\times 10^{11}\ {\rm yr}\left(\frac{M_\bullet/m_\star}{4\times 10^6}\right)\left(\frac{a}{1\ {\rm pc}}\right)^{3/2}, \tag{70b}$$

independent of the density of perturbers. Hopman & Alexander (2006b) note that this time falls below the standard relaxation time (Equation (8)) at a distance 0.1–0.5 pc from SgrA*. This suggests that resonant relaxation may reduce somewhat the timescale for isotropization compared with the values computed in Section 4.

The counter-intuitive result that $t_{\rm RR}$ is independent of the density of perturbing stars (Equation (70b)) is due to the fact that the coherence time $t_{\rm precess}$ becomes long as N becomes small, allowing even small torques to build up for long times. In the core models discussed here, N can be essentially zero, and other processes would likely begin to dominate the precession rate. For instance, a nuclear bar (e.g., Alard 2001) would generate a non-axisymmetric component to the gravitational potential in its interior, setting an upper limit to the precession time and reducing the effectiveness of resonant relaxation compared with the expressions given above as $N \to 0$.

Massive perturbers: Equation (15) says that the rate of gravitational scattering by a background population of perturbers scales as

$$n_p\langle m_p^2\rangle, \tag{71}$$

where n_p is the number density of perturbers of individual mass m_p and the brackets denote a number-weighted average. This expression ignores differences in the velocity distribution between the different populations, which is reasonable if the relaxation time is long and/or if the perturbers were recently formed. Perets et al. (2007) noted that the mass spectrum of giant molecular clouds implies that they should dominate the scattering rate beyond a few parsecs from SgrA*, reducing the relaxation time in this region by as much as several orders of magnitude. Inside ∼5 pc, they suggested that gas clumps in the circumnuclear gas disk, with masses 10^3–$10^5\ M_\odot$, might be similarly important.

Massive perturbers beyond ∼1 pc would affect the distribution of stars near the SMBH in two distinct ways (Perets et al. 2007). (1) Deflection of unbound (with respect to the SMBH) stars onto radial orbits would fill in some of the phase-space volume that was evacuated by formation of the core. This population would have a spatial distribution $n \sim r^{-1/2}$, similar to that of the pre-existing core. (2) Three-body interactions of field binaries deflected by massive perturbers can create a population of bound stars around the SMBH, initially on very eccentric orbits. The radial distribution of these bound stars will reflect the semimajor axis distribution of the parent binary population, which is uncertain. The capture rate is estimated to be as large as $\sim 10^{-4}$ yr^{-1} in the inner parsec; the accumulated mass could therefore potentially exceed the number of stars in the evolutionary models considered here. These arguments, while very approximate, suggest that massive perturbers could compete with stellar-mass perturbers in terms of refilling an evacuated core.

In a general way, the fact that the Milky Way *does* contain a low-density core implies an upper limit on the effectiveness of any relaxation process, particularly those that change orbital energies.

6.4. Extreme-mass-ratio Inspirals

The inspiral of compact remnants (stellar-mass BHs, NSs, and WDs) into an SMBH is accompanied by the emission of gravitational waves with frequencies that will be detectable by the *Laser Interferometer Space Antenna* (*LISA*; Sigurdsson & Rees 1997; Barack & Cutler 2004; Amaro-Seoane et al. 2007). Event rates of these extreme-mass-ratio inspirals (EMRIs) are generally computed assuming that the stars and stellar remnants are distributed in a relaxed, multi-mass density cusp (Hils & Bender 1995; Hopman & Alexander 2005; Hopman 2009). In such a cusp, the density of solar-mass stars follows $n \sim r^{-1.5}$ while the $10\ M_\odot$ BHs have a steeper dependence, $n \sim r^{-1.75} - r^{-2}$. The radius at which the mass density of BHs rises above that of the less massive objects depends on the choices made for the mass function, and (in the time-dependent models) the initial spatial distributions and the elapsed time. Typically, $\rho_{\rm BH} > \rho_\star$ inside 0.01–0.1 pc (Freitag et al. 2006a; Hopman & Alexander 2006a). The EMRI event rate is dominated by BHs (as opposed to NSs or WDs) due to their high masses and high mass densities. Most of the signal is contributed by BHs inside $\sim 10^{-2}$ pc (e.g., Hopman & Alexander 2006a, Figure 2).

Here, we estimate BH inspiral rates for models of the NSC that include a core. A distribution-function-based approach, similar to what was used above to compute stellar tidal disruption rates, would require an additional Monte Carlo calculation to estimate the probability that a star on a loss cone orbit will evade being scattered directly into the SMBH before emitting gravitational waves. Instead, we follow the more approximate treatments in Hils & Bender (1995), Hopman & Alexander (2005), and Ivanov

(2002) based only on the density profiles of the two components. We first derive an expression for the inspiral rate based on the observed stellar distribution, Figures 1 and 3. Event rates predicted by the evolving, two-component models of Section 5 are then computed.

Gravitational-wave emission is dominated by BHs that are scattered into the SMBH from orbits with $a \lesssim a_{\rm crit}$, where $a_{\rm crit}$ is the orbital radius such that the decay time due to emission of gravitational waves equals the time for the BH to be scattered in or out of the loss cone by stars or by other BHs. The angular momentum of a loss cone orbit is

$$J_{\rm lc} \approx \frac{4GM_\bullet}{c}. \quad (72)$$

Stars with $a \lesssim r_{\rm crit}$ can avoid scattering for a time long enough to spiral in via emission of gravitational waves. The inspiral rate is approximately

$$\dot{N}_{\rm GW} \approx \int_0^{a_{\rm crit}} \frac{f_{\rm BH}(a)N(a)}{t_r(a)\ln\Theta} da, \quad (73)$$

where $N(a)da$ is the number of stars and BHs with semimajor axes a to a+da, $f_{\rm BH} \leqslant 1$ is the fraction of objects which are BHs, and $\Theta = J_c/J_{\rm lc}$.

The gravitational-wave inspiral time for an eccentric orbit, $J \ll J_c$, is (Hopman & Alexander 2005)

$$t_{\rm GW} = \frac{3\times 2^{14}}{85}\frac{\sqrt{GM_\bullet a}}{c^2}\frac{M_\bullet}{m_{\rm BH}}\left(\frac{J}{J_{\rm lc}}\right)^7, \quad (74)$$

where $m_{\rm BH}$ is the mass of a stellar BH. The critical radius is defined as the radius where $t_{\rm GW} = t_{\rm lc}$ with

$$t_{\rm lc} = \left(\frac{J_{\rm lc}}{J_c}\right)^2 t_r, \quad (75)$$

the diffusion time into the loss cone. Combining Equations (74) and (75) and identifying the relaxation time on an orbit with its value at $r = a$ gives an implicit relation for $a_{\rm crit}$:

$$\frac{85}{3}\frac{m_{\rm BH}}{M_\bullet}\left(\frac{GM_\bullet}{a_{\rm crit}^3}\right)^{1/2} t_r(a_{\rm crit}) = 2^{10} \quad (76)$$

the solution to which determines the upper limit to the rate integral (Equation (73)).

For the relaxation time, we use the estimate plotted in Figure 3 for the Galactic center, which was based on the parametric model fit to the number counts, Figure 1, with $n \propto r^{-1/2}$ enforced at small radii. This is the flattest central dependence consistent with an isotropic f for the stars (Section 3), and is also similar to what is found in the evolving models (Sections 4 and 5). The relaxation time plotted in Figure 3 can be written as

$$t_r(r) \approx 1\times 10^{10}\,{\rm yr}\left(\frac{\tilde{m}}{M_\odot}\right)^{-1}\left(\frac{r}{0.2\,{\rm pc}}\right)^{-1}, \quad r \lesssim 0.2\,{\rm pc}, \quad (77)$$

where $\tilde{m}$ is defined in Equation (15b) and accounts for the possibility that stellar BHs may contribute significantly to the density of scatterers. (Note however that this expression assumes a particular normalization for the *total* mass density; this assumption will be relaxed below). In our two-component model, $\tilde{m}$ is fixed by $f_{\rm BH}$:

$$\frac{\tilde{m}}{m} = \frac{1 - f_{\rm BH} + f_{\rm BH}m_{\rm BH}^2/m^2}{1 - f_{\rm BH} + f_{\rm BH}m_{\rm BH}/m} \approx \frac{1+99f_{\rm BH}}{1+9f_{\rm BH}} \quad (78)$$

with m the stellar mass; the last relation assumes $m_{\rm BH} = 10m$.

Substituting Equation (77) into Equation (76) gives for the critical radius

$$a_{\rm crit} \approx 0.08\,{\rm pc}\left(\frac{\tilde{m}}{m_{\rm BH}}\right)^{-0.4}. \quad (79)$$

For $\tilde{m}/m_{\rm BH} = 0.1(0.5)1$, $a_{\rm crit}/{\rm pc} = 0.2(0.11)0.08$. These are somewhat larger than the critical radii computed assuming a relaxed density cusp ($a_{\rm crit} \approx 10^{-2}$ pc) but are still small compared with the observed core radius of ∼0.5 pc.

The event rate (Equation (73)) becomes

$$\dot{N}_{\rm GW} \approx 3\times 10^2\,{\rm Gyr}^{-1} f_{\rm BH}\left(\frac{\tilde{m}}{m_{\rm BH}}\right)^{-0.4}\frac{N_{0.1}/10^4}{\ln\Theta/5}, \quad (80)$$

where $N_{0.1}$ is the number of stars and BHs inside 0.1 pc; the density normalization assumed in making Figure 3, Equation (10), implies $N_{0.1} \approx 8.6\times 10^3$.

Setting $f_{\rm BH} = 0.001$ and $\tilde{m} \approx 1\,M_\odot$ in this formula gives an estimate of the inspiral rate for an unsegregated model in which the BHs follow the same density profile as the observed stars. Not surprisingly, the resultant rate is very low, $\dot{N} \approx 1$ Gyr^{-1}. If instead $f_{\rm BH}$ is set to the higher values found in the steady-state models, i.e., $f_{\rm BH} = 0.01(0.05)0.1$, Equation (80) gives $\dot{N}_{\rm GW} \approx 2(9)15$ Gyr^{-1}. These rates are still 1–2 orders of magnitude lower than those in the steady-state models, due to the very different *total* densities assumed at the relevant radii; for instance, Hopman & Alexander (2006a) find $\dot{N}_{\rm GW} \approx 300$ Gyr^{-1} in models that have $0.01 \lesssim f_{\rm BH} \lesssim 0.1$ at $r \approx a_{\rm crit}$. The magnitude of the difference is at first sight surprisingly small given that the steady-state models have total densities at 10^{-3} to 10^{-2} pc that are orders of magnitude higher than here. The reason is that the longer relaxation time in the core models implies a ∼10× larger value of $a_{\rm crit}$ and a ∼10^3× larger volume from which inspirals can occur (e.g., Hopman & Alexander 2005).

In the time-dependent models of Section 5, not only are total densities smaller than in the steady-state models, but $f_{\rm BH}$ also remains well below its value in a mass-segregated cusp until late times. Figure 18 shows BH inspiral rates computed in the same way as above, using the densities of stars and BHs in the time-dependent models. In these models, the BHs have initially the same spatial distribution as the stars; as the stellar core shrinks, the BHs "follow" it inward, increasing both their density near the center and their relative density with respect to the stars (Figure 16). By the time the stellar core shrinks to its observed value of ∼0.5 pc, the BH density at $r \lesssim a_{\rm crit}$ is still much lower than in the steady-state models and $\dot{N}_{\rm GW}$ is also correspondingly lower.

It must be emphasized that these evolutionary models are idealized and that one could imagine other, reasonable initial conditions that would produce rather different rates after 10 Gyr. For instance, the distribution of BHs might have exhibited some degree of segregation even at early times. The main point to be made here is that in models for the NSC that contain a core, $\dot{N}_{\rm GW}$ could plausibly be as much as 10–100 times lower than in models based on a steady-state, mass-segregated density cusp.

6.5. Inspiral of an IMBH

IMBHs, with masses of 10^2–10^3 $M_\odot$, may form in dense star clusters through runaway mergers of massive stars (Portegies

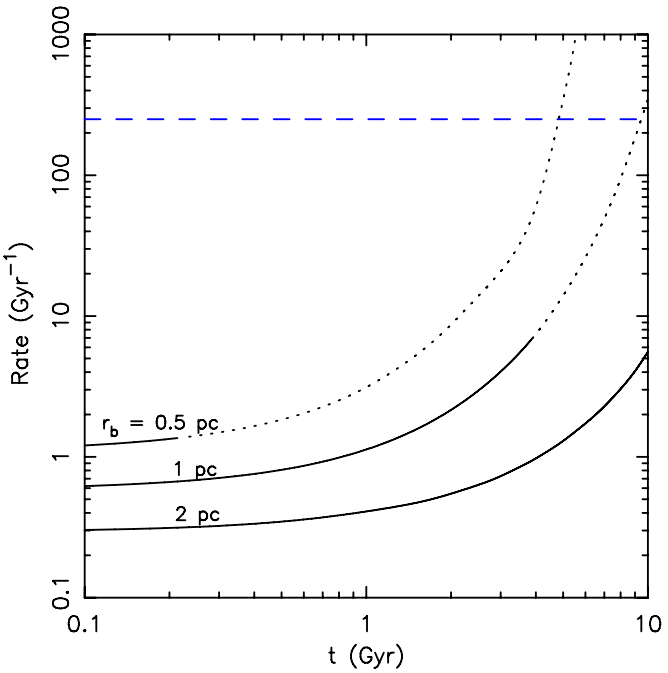

Figure 18. Evolution of the BH inspiral rate in the models of Figure 16. The solid part of each curve terminates at the time when the stellar core radius is 0.5 pc. The dashed (blue) line shows the event rate computed by Hopman & Alexander (2006a) in steady-state, mass-segregated models (cf. their Figure 2).
(A color version of this figure is available in the online journal.)

Zwart & McMillan 2002; Freitag et al. 2006b). Inspiral of an IMBH into the Galactic center is usually modeled assuming that the dynamical friction force originates in a stellar density cusp with $\rho \sim r^{-\gamma}$, $1.5 \lesssim \gamma \lesssim 2$ (Baumgardt et al. 2006; Matsubayashi et al. 2008; Löckmann & Baumgardt 2008). In these circumstances, inspiral continues until the IMBH reaches a distance from SgrA* such that the enclosed stellar mass is roughly equal to $m_{\rm IMBH}$, or 10^{-3} pc $\lesssim r \lesssim 10^{-2}$ pc.

If there is a pre-existing core in the stellar distribution, inspiral would stall at roughly 1/2 the core radius, or ∼0.25 pc in the case of the Galactic center (Figure 12), independent of the IMBH mass. Furthermore, as noted above, the orbital eccentricity of the IMBH would not be expected to decrease strongly during the inspiral.

Merritt et al. (2009) and Gualandris & Merritt (2009) noted one consequence of a "stalled" IMBH on an eccentric orbit: the IMBH very efficiently randomizes the orbits of ambient stars, producing a nearly "thermal" distribution of orbital eccentricities, $N(<e) \sim e^2$, on Myr timescales. Merritt et al. (2009) postulated stalling radii inside ∼0.1 pc in order to explain the observed distribution of the S-star orbits (Ghez et al. 2008; Gillessen et al. 2009). The somewhat larger stalling radii made plausible here suggest that IMBHs might be lurking on somewhat wider orbits, roughly the size of the two stellar disks at 0.1 pc $\lesssim r \lesssim$ 0.5 pc (Paumard et al. 2006; Lu et al. 2009; Bartko et al. 2009a). As shown by Levin et al. (2005) and Berukoff & Hansen (2006), an IMBH at these radii could play a role in truncating the stellar disks and scattering disk stars onto inclined and eccentric orbits. Those authors assumed efficient inspiral of the IMBHs, which limited the time over which interactions could occur. If orbital decay stalls at distances of ∼0.2 pc, dynamical interactions with disk stars could be prolonged indefinitely, potentially resulting in much greater changes in the stellar orbits.

An inspiralling IMBH also ejects stars and stellar remnants via three-body interactions with the IMBH/SMBH binary. Some of these stars receive kicks greater than $\sim 10^3$ km s^{-1}, allowing them to escape into the Galactic halo as HVSs (Yu & Tremaine 2003). Simulations of this process (Levin 2006; Baumgardt et al. 2006; Löckmann & Baumgardt 2008) also typically assume a steep density cusp for the stars. The resulting rate of ejection of HVSs increases rapidly with time as the IMBH spirals in, peaking when the IMBH reaches its (small) stalling radius of ∼0.01 pc, then falling off due to the local depletion of stars. The stellar density at this radius is assumed to be $\gtrsim 10^8\, M_\odot$ pc^{-3} initially, roughly the density implied by the (coreless) power-law model of Equation (12).

In the core models considered here, the rate of production of HVSs would be much smaller than in the relaxed models due to the lower stellar densities inside ∼1 pc. In addition, the IMBH would stall at a larger radius of ∼0.2 pc. The density at this radius is $\lesssim 10^6\, M_\odot$ pc^{-3}, resulting in a $\sim 10^2$ times smaller rate of escapers than the peak values obtained during infall in models with a steep cusp, i.e., 0.1–1 Myr^{-1}. On the other hand, at these low rates, ejections by the IMBH would hardly affect the ambient stellar density and the production of HVSs could continue indefinitely at an approximately constant rate. Production of ∼10 HVSs would therefore require a span of ∼10–100 Myr; in fact the observed span of travel times for escaping HVSs is $\sim 2 \times 10^8$ yr (Brown et al. 2007), roughly consistent with this crude estimate.

6.6. Dynamical Interactions that Postulate a High Density of Stellar Black Holes

A dense cluster of stellar-mass BHs has been invoked as a potential solution to a number of other problems of collisional dynamics at the Galactic center. Examples include: (1) removing stellar envelopes via physical collisions between BHs and stars (e.g., Dale et al. 2009), (2) randomizing the orbits of young stars via gravitational scattering off of BHs (e.g., Perets et al. 2009), and (3) production of HVSs through encounters with BHs (e.g., O'Leary & Loeb 2008). Typically $n_{\rm bh} \sim r^{-2}$ is assumed, as in the relaxed, mass-segregated models, implying a mass in BHs of $\sim 10^4\, M_\odot$ within one 0.1 pc. The 10–100 times lower BH densities found in some of the evolutionary models presented here would imply correspondingly lower rates of interaction.

We note that alternative mechanisms exist for solving many of these outstanding problems. For instance, a single IMBH can randomize the orbits of young stars even more efficiently than a BH cusp (Merritt et al. 2009).

6.7. Cores and Nuclear Star Clusters

As shown above (Section 4), the relaxation time at the Galactic center is short enough that a parsec-scale core will shrink appreciably over the course of 10 Gyr. What is the connection between such a hypothesized initial core, and the cores that are observed in spheroids brighter than $M_B \approx -19.5$ (Côté et al. 2007)?

The classification of spheroids into cored or coreless families is based on data with an angular resolution of ∼0.″1, corresponding to a linear size of ∼1 pc at a distance of the Virgo galaxy cluster. Neither the current core at the center of the Milky Way, nor the larger initial core postulated here, would be easily discernable at this distance. Instead, the Milky Way would likely be classified as a galaxy with an NSC: its luminosity profile is relatively flat outside ∼10 pc and rises steeply inside (Launhardt

et al. 2002; Schödel et al. 2008; Graham & Spitler 2009). The observed core sits atop that star cluster. NGC 205 also has both an NSC and a core; the core radius is $\sim 0\farcs12 \approx 0.5$ pc (Merritt 2009), making it very similar to the Milky Way core (although it is not clear that NGC 205 contains an SMBH; Valluri et al. 2005).

Many other galaxies with NSCs could also contain undetected cores. Bright young stars, like those at the center of the Milky Way, M31, and other galaxies with NSCs (van der Marel et al. 2007), would tend to mask the existence of a core in the old population, as indeed they did until very recently at the Galactic center.

While most NSCs are too small for their internal structure to be resolved, the half-mass relaxation time $t_{\rm nuc}$ can be reliably estimated for many, and its mean dependence on host galaxy (not NSC) luminosity is

$$\log_{10}(t_{\rm nuc}/{\rm yr}) = 9.38 - 0.434(M_B + 16) \quad (81)$$

(Merritt 2009) where M_B is the absolute blue magnitude of the bulge component. If we assume that galaxies with NSCs also contain SMBHs, and that the relaxation time at $r_{\rm infl}$ is no greater than its value at the NSC half-light radius, then relaxation times drop below 10 Gyr at $M_B \approx -17$, slightly fainter than the estimated luminosity of the Milky Way bulge, $M_B = -17.6$ (Marconi & Hunt 2003).

These arguments suggest that cores comparable in size to SMBH influence radii might exist in other galaxies with NSCs. Relaxation times in the NSCs are expected to be short enough that such cores could shrink appreciably in 10 Gyr.

7. CONCLUSIONS

1. The distribution of old stars at the Galactic center exhibits a low-density core of radius $\sim$0.5 pc. The deprojected central density is poorly constrained but is consistent with zero.
2. Assuming that the old stars trace the mass in the inner parsec, the two-body relaxation time (for solar-mass stars) is nowhere shorter than $\sim$5 Gyr. The relaxation time at the influence radius of SgrA*, $r_{\rm infl} \approx 2.5$ pc, is robustly estimated to be 20–30 Gyr.
3. Reproducing the observed distribution of old stars with a steady-state distribution function requires a strongly truncated phase-space density at low energies and/or low angular momenta. If the stellar density increases more slowly than $r^{-0.5}$ toward SgrA*, the velocity distribution must be anisotropic in the inner parsec, with a deficit of eccentric orbits ("anisotropic core"). Otherwise the distribution function can be isotropic ("isotropic core").
4. Anisotropic-core models evolve toward isotropy on a Gyr timescale. In the process, the core radius decreases only slightly. The observed (small) degree of anisotropy at the Galactic center is consistent with such models at both early and late times.
5. On a longer timescale, gravitational encounters produce changes in stellar orbital energies, causing a pre-existing core to shrink. Initial core radii in the range 1–1.5 pc evolve, after 10 Gyr, to cores of the currently observed size.
6. The dynamical friction force acting on an inspiralling massive body falls essentially to zero at roughly 1/2 the stellar core radius. This results in an accumulation of 10 $M_\odot$ BHs in a shell just inside the stellar core. Orbital decay of an IMBH would also be expected to stall at this radius, rather than the much smaller stalling radius expected in a dense stellar cusp.
7. The expected density of 10 $M_\odot$ BHs in the inner parsec depends sensitively on their initial distribution and on the elapsed time, but may be substantially lower than in models that assume the absence of a stellar core. Rates of gravitational-wave-driven inspirals of stellar-mass BHs are 1–2 orders of magnitude lower than predicted by steady-state models with a mass-segregated density cusp.

Don Figer, Sungsoo Kim, Rainer Schödel, and especially Tal Alexander read early versions of this paper and provided helpful comments and corrections. Useful discussions with M. Messineo, H. Perets, and E. Vassiliev are also acknowledged. The author was supported by grants AST-0807910 (NSF) and NNX07AH15G (NASA).

APPENDIX

ORBITAL DISTRIBUTIONS IN A CORE AROUND AN SMBH

In the context of "isotropic-core" models, we derive the distribution of orbital eccentricities that one would measure at a point inside the core and near to the SMBH.

We assume that $r \ll r_b \ll r_{\rm infl}$, where r is the point of observation, r_b defines the truncation energy through $E_b = \phi(r_b)$, and $r_{\rm infl}$ is the SMBH influence radius.

Assuming a power law in space density outside the core, the phase-space density is given by Equation (50),

$$\begin{aligned} f(E) &= f_0|E|^{\gamma-3/2}, \quad E > E_b \\ &= 0, \quad E \leqslant E_b, \end{aligned} \quad (A1)$$

where we have assumed that the gravitational potential is

$$\phi(r) = -\frac{GM_\bullet}{r}, \quad (A2)$$

i.e., that $r \ll r_{\rm infl}$.

The velocity space volume element is

$$d^3\mathbf{v} = 4\pi v^2 dv \sin\theta d\theta, \quad (A3)$$

where θ is the angle between $\mathbf{v}$ and $\mathbf{r}$ and $0 \leqslant \theta \leqslant \pi/2$. Using

$$E = \frac{1}{2}v^2 + \phi(r) = -\frac{GM_\bullet}{2a}, \quad (A4a)$$

$$J = rv\sin\theta = \sqrt{1-e^2}\,\frac{GM_\bullet}{\sqrt{-2E}}, \quad (A4b)$$

this becomes

$$d^3\mathbf{v} = \frac{G^2M_\bullet^2}{2r^2v_r}\frac{e}{a}dade, \quad (A5)$$

where $v_r = v\cos\theta$. The distribution of eccentricities at r is then given by the integration over a, or

$$\frac{dN}{de} \propto e\int_{r_b/2}^{r/(1-e)} \frac{da}{av_r} f(a). \quad (A6)$$

The lower limit is the semimajor axis of an orbit of energy E_b. The upper limit on a corresponds to an orbit of eccentricity e with periapse at r. The integral is zero unless

$$\frac{r}{1-e} > \frac{r_b}{2} \quad (A7)$$

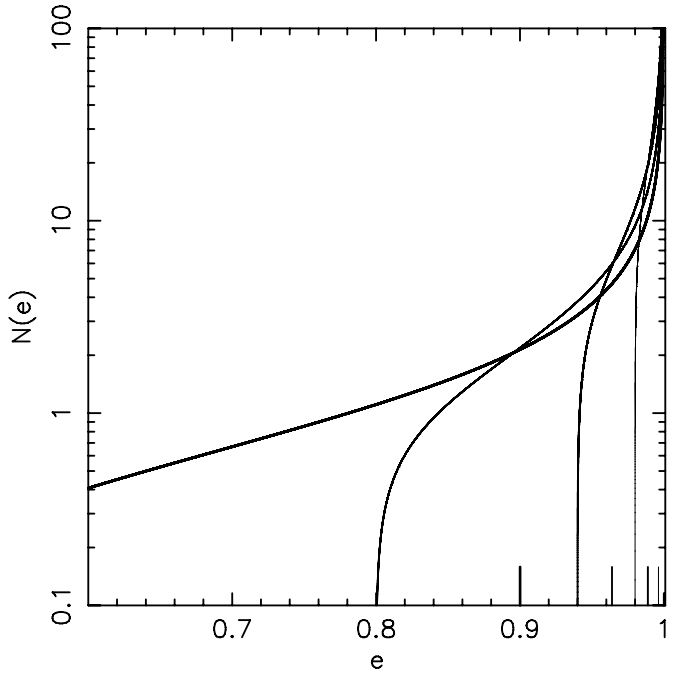

Figure 19. Distribution of orbital eccentricities that would be measured at a given distance from the SMBH in an "isotropic-core" model. The density profile outside the core is $n \propto r^{-1.8}$. Curves show $N(e)$ at $r = (0.3, 0.1, 0.03, 0.01) \times r_b$; line width decreases with decreasing r. The vertical tick marks show $\langle e \rangle$ for each curve.

or

$$e > 1 - 2\frac{r}{r_b}. \tag{A8}$$

Writing

$$v_r^2 = \frac{GM_\bullet}{r}\left[2 - \frac{r}{a} - (1-e^2)\frac{a}{r}\right] \tag{A9}$$

and $f(a) \propto a^{3/2-\gamma}$, this becomes

$$\frac{dN}{de} = N_0 e \int_{r_b/2}^{r/(1-e)} da \frac{a^{1/2-\gamma}}{\sqrt{2 - \frac{r}{a} - (1-e^2)\frac{a}{r}}}, \quad e > 1 - 2\frac{r}{r_b}. \tag{A10}$$

Defining a new variable $x = (1-e)\frac{a}{r}$, this takes on the simpler form

$$\frac{dN}{de} = N_0 e (1-e)^{3/2-0\gamma}(1+e)^{-1/2}\int_{x_1}^1 dx \frac{x^{1-\gamma}}{\sqrt{(1-x)\left(x - \frac{1-e}{1+e}\right)}},$$

$$x_1 = (1-e)\frac{r_b}{2r},$$

$$1 \geqslant e \geqslant 1 - \frac{2r}{r_b}. \tag{A11}$$

Figure 19 shows $N(e)$, normalized to unit total number, at radii of

$$0.3, 0.1, 0.03, 0.01 \tag{A12}$$

times r_b assuming $\gamma = 1.8$. Also shown are the mean eccentricities at each radius. $N(e)$ approximates a delta function at $e = 1$ for $r \ll r_b$, since the only orbits that reach into these small radii must be very eccentric.

Proceeding as before, the distribution of orbital semimajor axes at r is

$$N(a) = 2^{3/2-\gamma}(\gamma - 3/2) r_b^{-1}\left(\frac{a}{r_b}\right)^{1/2-\gamma}, \quad a \geqslant r_b/2, \tag{A13}$$

where $e = 1$ and $r \ll r_b$ have also been assumed. The mean value of a is

$$\frac{\langle a \rangle}{r_b} = \frac{1}{2}\frac{\gamma - 3/2}{5/2 - \gamma} \tag{A14}$$

and for $\gamma = 1.8$,

$$\frac{\langle a \rangle}{r_b} = 0.214. \tag{A15}$$

Setting $r_b \approx 0.5$ pc, the expected orbit should have a semimajor axis of $\sim$0.1 pc and an eccentricity near 1.

REFERENCES

Alard, C. 2001, A&A, 379, L44
Alexander, T. 1999, ApJ, 527, 835
Alexander, T. 2005, Phys. Rep., 419, 65
Alexander, T., & Hopman, C. 2009, ApJ, 697, 1861
Allen, D. A., Hyland, A. R., & Hillier, D. J. 1990, MNRAS, 244, 706
Amaro-Seoane, P., Gair, J. R., Freitag, M., Miller, M. C., Mandel, I., Cutler, C. J., & Babak, S. 2007, Class. Quantum Grav., 24, 113
Bahcall, J. N., & Wolf, R. A. 1976, ApJ, 209, 214
Bahcall, J. N., & Wolf, R. A. 1977, ApJ, 216, 883
Bailey, V. C., & Davies, M. B. 1999, MNRAS, 308, 257
Barack, L., & Cutler, C. 2004, Phys. Rev. D, 69, 082005
Bartko, H., et al. 2009a, ApJ, 697, 1741
Bartko, H., et al. 2009b, ApJ, 708, 834
Baumgardt, H., Gualandris, A., & Portegies Zwart, S. 2006, MNRAS, 372, 174
Becklin, E. E., & Neugebauer, G. 1968, ApJ, 151, 145
Berukoff, S. J., & Hansen, B. M. S. 2006, ApJ, 650, 901
Blum, R. D., Ramírez, S. V., Sellgren, K., & Olsen, K. 2003, ApJ, 597, 323
Boylan-Kolchin, M., Ma, C.-P., & Quataert, E. 2004, ApJ, 613, L37
Brown, W. R., Geller, M. J., Kenyon, S. J., Kurtz, M. J., & Bromley, B. C. 2007, ApJ, 671, 1708
Buchholz, R. M., Schödel, R., & Eckart, A. 2009, A&A, 499, 483
Chakrabarty, D., & Saha, P. 2001, AJ, 122, 232
Cohn, H. 1979, ApJ, 234, 1036
Cohn, H. 1980, ApJ, 242, 765
Cohn, H., & Kulsrud, R. M. 1978, ApJ, 226, 1087
Côté, P., et al. 2007, ApJ, 671, 1456
Dale, J. E., Davies, M. B., Church, R. P., & Freitag, M. 2009, MNRAS, 393, 1016
Davies, M. B., & King, A. 2005, ApJ, 624, L25
Davies, B., Origlia, L., Kudritzki, R.-P., Figer, D. F., Rich, R. M., & Najarro, F. 2009, ApJ, 694, 46
Do, T., Ghez, A. M., Morris, M. R., Lu, J. R., Matthews, K., Yelda, S., & Larkin, J. 2009, ApJ, 703, 1323
Eckart, A., Genzel, R., Ott, T., & Schödel, R. 2002, MNRAS, 331, 917
Eddington, A. S. 1916, MNRAS, 76, 572
Eisenhauer, F., et al. 2005, ApJ, 628, 246
Faber, S. M., et al. 1997, AJ, 114, 1771
Ferrarese, L., et al. 2006, ApJS, 164, 334
Figer, D. F. 2008, arXiv:0803.1619
Figer, D. F., Rich, R. M., Kim, S. S., Morris, M., & Serabyn, E. 2004, ApJ, 601, 319
Figer, D. F., et al. 2000, ApJ, 533, L49
Figer, D. F., et al. 2003, ApJ, 599, 1139
Forrest, W. J., Shure, M. A., Pipher, J. L., & Woodward, C. E. 1987, in AIP Conf. Proc. 155, The Galactic Center (Berlin: Springer), 153
Frank, J., & Rees, M. J. 1976, MNRAS, 176, 633
Freitag, M., Amaro-Seoane, P., & Kalogera, V. 2006a, ApJ, 649, 91
Freitag, M., Gürkan, M. A., & Rasio, F. A. 2006b, MNRAS, 368, 141
Genzel, R., Pichon, C., Eckart, A., Gerhard, O. E., & Ott, T. 2000, MNRAS, 317, 348
Genzel, R., Thatte, N., Krabbe, A., Kroker, H., & Tacconi-Garman, L. E. 1996, ApJ, 472, 153
Genzel, R., et al. 2003, ApJ, 594, 812
Ghez, A. M., Klein, B. L., Morris, M., & Becklin, E. E. 1998, ApJ, 509, 678
Ghez, A. M., et al. 2008, ApJ, 689, 1044
Gillessen, S., Eisenhauer, F., Trippe, S., Alexander, T., Genzel, R., Martins, F., & Ott, T. 2009, ApJ, 692, 1075
Graham, A. W. 2004, ApJ, 613, L33
Graham, A. W., & Spitler, L. R. 2009, MNRAS, 397, 2148
Gualandris, A., & Merritt, D. 2008, ApJ, 678, 780
Gualandris, A., & Merritt, D. 2009, ApJ, 705, 361

Haller, J. W., Rieke, M. J., Rieke, G. H., Tamblyn, P., Close, L., & Melia, F. 1996, ApJ, 456, 194
Hénon, M. 1961, Ann. Astrophys., 24, 369
Hils, D., & Bender, P. L. 1995, ApJ, 445, L7
Hopman, C. 2009, Class. Quantum Grav., 26, 094028
Hopman, C., & Alexander, T. 2005, ApJ, 629, 362
Hopman, C., & Alexander, T. 2006a, ApJ, 645, L133
Hopman, C., & Alexander, T. 2006b, ApJ, 645, 1152
Ivanov, P. B. 2002, MNRAS, 336, 373
King, I. 1962, AJ, 67, 471
Krabbe, A., Genzel, R., Drapatz, S., & Rotaciuc, V. 1991, ApJ, 382, L19
Krabbe, A., et al. 1995, ApJ, 447, L95
Launhardt, R., Zylka, R., & Mezger, P. G. 2002, A&A, 384, 112
Levin, Y. 2006, ApJ, 653, 1203
Levin, Y., Wu, A., & Thommes, E. 2005, ApJ, 635, 341
Lightman, A. P., & Shapiro, S. L. 1977, ApJ, 211, 244
Löckmann, U., & Baumgardt, H. 2008, MNRAS, 384, 323
Lu, J. R., Ghez, A. M., Hornstein, S. D., Morris, M. R., Becklin, E. E., & Matthews, K. 2009, ApJ, 690, 1463
Marconi, A., & Hunt, L. K. 2003, ApJ, 589, L21
Matsubayashi, T., Makino, J., & Ebisuzaki, T. 2008, ApJ, 656, 879
McGinn, M. T., Sellgren, K., Becklin, E. E., & Hall, D. N. B. 1989, ApJ, 338, 824
Merritt, D. 2004, Phys. Rev. Lett., 92, 201304
Merritt, D. 2006a, ApJ, 648, 976
Merritt, D. 2006b, Rep. Prog. Phys., 69, 2513
Merritt, D. 2009, ApJ, 694, 959
Merritt, D., Gualandris, A., & Mikkola, S. 2009, ApJ, 693, L35
Merritt, D., Milosavljević, M., Favata, M., Hughes, S. A., & Holz, D. E. 2004, ApJ, 607, L9
Merritt, D., Milosavljević, M., Verde, L., & Jimenez, R. 2002, Phys. Rev. Lett., 88, 191301
Merritt, D., & Poon, M. Y. 2004, ApJ, 606, 788
Merritt, D., & Wang, J. 2005, ApJ, 621, L101
Mezger, P. G., Zylka, R., Philipp, S., & Launhardt, R. 1999, A&A, 348, 457
Milosavljević, M., & Merritt, D. 2001, ApJ, 563, 34
Milosavljević, M., & Merritt, D. 2003, ApJ, 596, 860
Miralda-Escudé, J., & Gould, A. 2000, ApJ, 545, 847
Morris, M. 1993, ApJ, 408, 496
Muno, M. P., Pfahl, E., Baganoff, F. K., Brandt, W. N., Ghez, A., Lu, J., & Morris, M. R. 2005, ApJ, 622, L113
Murphy, B. W., Cohn, H. N., & Durisen, R. H. 1991, ApJ, 370, 60
Nayakshin, S., & Sunyaev, R. 2005, MNRAS, 364, L23
O'Leary, R. M., & Loeb, A. 2008, MNRAS, 383, 86
Paumard, T. 2008, J. Phys. Conf. Ser., 131, 012009
Paumard, T., et al. 2006, ApJ, 643, 1011
Peebles, P. J. E. 1972, Gen. Rel. Gravit., 3, 63
Peirani, S., Kay, S., & Silk, J. 2008, A&A, 479, 123
Perets, H. B., Hopman, C., & Alexander, T. 2007, ApJ, 656, 709
Perets, H. B., Gualandris, A., Kupi, G., Merritt, D., & Alexander, T. 2009, ApJ, 702, 884
Philipp, S., Zylka, R., Mezger, P. G., Duschl, W. J., Herbst, T., & Tuffs, R. J. 1999, A&A, 348, 768
Poon, M. Y., & Merritt, D. 2001, ApJ, 549, 192
Portegies Zwart, S. F., Baumgardt, H., McMillan, S. L. W., Makino, J., Hut, P., & Ebisuzaki, T. 2006, ApJ, 641, 319
Portegies Zwart, S. F., & McMillan, S. L. W. 2002, ApJ, 576, 899
Quinlan, G. D. 1996, New Astron., 1, 255
Rauch, K. P., & Tremaine, S. 1996, New Astron., 1, 149
Schödel, R., Merritt, D., & Eckart, A. 2008, J. Phys. Conf. Ser., 131, 012044
Schödel, R., Merritt, D., & Eckart, A. 2009, Astron. Ap., 502, 91
Schödel, R., et al. 2007, A&A, 469, 125
Scoville, N. Z., Stolovy, S. R., Rieke, M., Christopher, M., & Yusef-Zadeh, F. 2003, ApJ, 594, 294
Sellgren, K., McGinn, M. T., Becklin, E. E., & Hall, D. N. 1990, ApJ, 359, 112
Serabyn, E., & Morris, M. 1996, Nature, 382, 602
Shapiro, S. L., & Marchant, A. B. 1978, ApJ, 225, 603
Sigurdsson, S., & Rees, M. J. 1997, MNRAS, 284, 318
Spitzer, L. 1987, Dynamical Evolution of Globular Clusters (Princeton, NJ: Princeton Univ. Press)
Szell, A., Merritt, D., & Kevrekidis, I. G. 2005, Phys. Rev. Lett., 95, 081102
Takahashi, K. 1997, PASJ, 49, 547
Terzić, B., & Graham, A. W. 2005, MNRAS, 362, 197
Tremaine, S. 1997, in Unsolved Problems in Astrophysics, ed. J. N. Bahcall & J. P. Ostriker (Princeton, NJ: Princeton Univ. Press), 137
Valluri, M., Ferrarese, L., Merritt, D., & Joseph, C. L. 2005, ApJ, 628, 137
van der Marel, R. P., Rossa, J., Walcher, C. J., Boeker, T., Ho, L. C., Rix, H.-W., & Shields, J. C. 2007, in IAU Symp. 241, Stellar Populations as Building Blocks of Galaxies, ed. A. Vazdekis & R. F. Peletier (Cambridge: Cambridge Univ. Press), 475
Wang, J., & Merritt, D. 2004, ApJ, 600, 149
Wyse, R. F. G. 2001, in ASP Conf. Ser. 230, Galaxy Disks and Disk Galaxies, ed. J. G. Funes, S. J. & E. M. Corsini (San Francisco, CA: ASP), 71
Yu, Q., & Tremaine, S. 2003, ApJ, 599, 1129
Zhu, Q., Kudritzki, R. P., Figer, D. F., Najarro, F., & Merritt, D. 2008, ApJ, 681, 1254